

RAMAN AND FOURIER TRANSFORM INFRARED SPECTROSCOPY
CHARACTERIZATION OF NICKEL SILICIDES

THESIS

Presented to the Graduate Council of
Texas State University – San Marcos
in Partial Fulfillment of
the Requirements

For the Degree

Master of SCIENCE

By

Anita René Acevedo, B.S.

San Marcos, Texas
May 2004

COPYRIGHT

by

Anita René Acevedo

2004

ACKNOWLEDGEMENTS

I would like to thank the members of my thesis committee, Dr. Heather Galloway and Dr. Wilhelmus Geerts. Their feedback was invaluable to the shaping of my thesis topic.

I am very thankful for Dr. David Donnelly, my thesis advisor, for his guidance and patience.

I would like to thank Lynette Ballast and Eduardo Dozal for the fabrication of the samples used for this project.

I am also very grateful for the support I have received from my family, especially my parents Reynaldo and Francine Acevedo.

Most of all I would like to thank God for all the blessings He has given me, including the completion of the requirements for my master's degree.

This manuscript was submitted on April 7, 2004.

TABLE OF CONTENTS

ACKNOWLEDGEMENTS.....	iv
LIST OF FIGURES.....	vi
ABSTRACT.....	viii
Chapter	
I INTRODUCTION	1
II THEORY	4
Formation and Structure of Nickel Silicide Contacts.....	4
Theory of Raman Spectroscopy.....	7
Raman Instrumentation.....	20
Theory of Infrared Spectroscopy.....	23
FTIR Instrumentation.....	24
III EXPERIMENT.....	28
IV DATA.....	29
V RESULTS.....	37
APPENDIX A: EIGENSTATES AND ENERGIES OF A QUANTUM HARMONIC OSCILLATOR.....	41
APPENDIX B: CRYSTAL STRUCTURES OF NICKEL SILICIDES.....	44
REFERENCES.....	50

LIST OF FIGURES

Figure 1. The salicide process.....	1
Figure 2. Thin film kinetics of nickel silicide growth.....	7
Figure 3. Energy levels involved in a Raman scattering event	10
Figure 4. Typical Raman spectrum of NiSi.....	13
Figure 5. Potential energy of atoms in a solid.....	13
Figure 6. Vibrations of isolated molecules.	15
Figure 7. Optical and acoustic phonons.....	16
Figure 8. Schematic of Raman spectrometer	22
Figure 9. The Michelson interferometer	24
Figure 10. Schematic of FTIR spectrometer.....	27
Figure 11. IR absorbance of n-doped, 380°C annealed sample.....	30
Figure 12. IR absorbance of p-doped, 380°C annealed sample.....	30
Figure 13. IR absorbance of n-doped, 450°C annealed sample.....	31
Figure 14. IR absorbance of p-doped, 450°C annealed sample.....	31

Figure 15. IR absorbance of n-doped, 850°C annealed sample.....	32
Figure 16. IR absorbance of p-doped, 850°C annealed sample.....	32
Figure 17. Raman spectrum of n-doped, 380°C annealed sample.....	34
Figure 18. Raman spectrum of p-doped, 380°C annealed sample.....	34
Figure 19. Raman spectrum of n-doped, 450°C annealed sample.....	35
Figure 20. Raman spectrum of p-doped, 450°C annealed sample.....	35
Figure 21. Raman spectrum of n-doped, 850°C annealed sample.....	36
Figure 22. Raman spectrum of p-doped, 850°C annealed sample.....	36
Figure 23. Typical phonon dispersion curve.....	40
Figure B-1. Crystal structure of Ni ₂ Si.....	44
Figure B-2. Crystal structure of NiSi.....	46
Figure B-3. Crystal structure of NiSi ₂	48

ABSTRACT

RAMAN AND FOURIER TRANSFORM INFRARED SPECTROSCOPY CHARACTERIZATION OF NICKEL SILICIDES

by

Anita René Acevedo, B.S.

Texas State University – San Marcos

May 2004

SUPERVISING PROFESSOR: DAVID DONNELLY

The purpose of this study was to identify nickel silicide phases which were produced by rapid thermal annealing (RTA) at different temperatures, to examine the dependence of nickel silicide growth on dopant species of the substrate, and to compare growth kinetics to previously observed growth patterns reported in literature. Six nickel-silicide thin film samples were prepared on eight-inch crystalline silicon wafers (100 surface) for the study. Prior to the preparation of the silicide films, all wafers received a dopant and dopant activation step. Three wafers received a boron dopant, and three wafers received a phosphorous dopant; dopant concentrations were 10^{15} cm^{-3} . Then a

19 nm thick layer of nickel metal was deposited onto all wafers. Finally, each wafer received one of three different RTA treatments to create the silicide layer. These treatments were all done for thirty seconds and differed only in the temperature chosen. These temperatures were: 380C, 450C, and 850C.

The Raman analysis was done at Advanced Micro Devices in the Process Characterization and Analysis Laboratory. The FTIR analysis was done at Texas State University in the laboratory of Dr. David Donnelly.

Peaks observed in the Raman spectra of the samples corresponded to previously reported peaks for NiSi. This enabled the identification of this silicide phase. However, growth kinetics differed from the thin film kinetics observed in other reports, which were expected to occur in this study. The silicides were expected to appear sequentially in the order: Ni₂Si, NiSi, NiSi₂. In contrast, the Raman spectra gathered from the samples suggested the growth of the NiSi layer occurred before all the nickel metal was consumed. In addition, the growth rate of nickel monosilicide showed a dependence on dopant species.

CHAPTER ONE:INTRODUCTION

Metal silicides that exhibit metallic behavior are used to form electrical contacts to the active regions of a transistor. The process of forming these contacts, called “silicidation”, typically begins with deposition of metal onto a patterned wafer followed by a rapid thermal anneal (RTA) of the entire wafer.¹ A commonly used technique known as the “salicide” (self-aligned silicide) process forms silicide contacts to the source, drains, and gate in the same step. This process is shown in Figure 1.

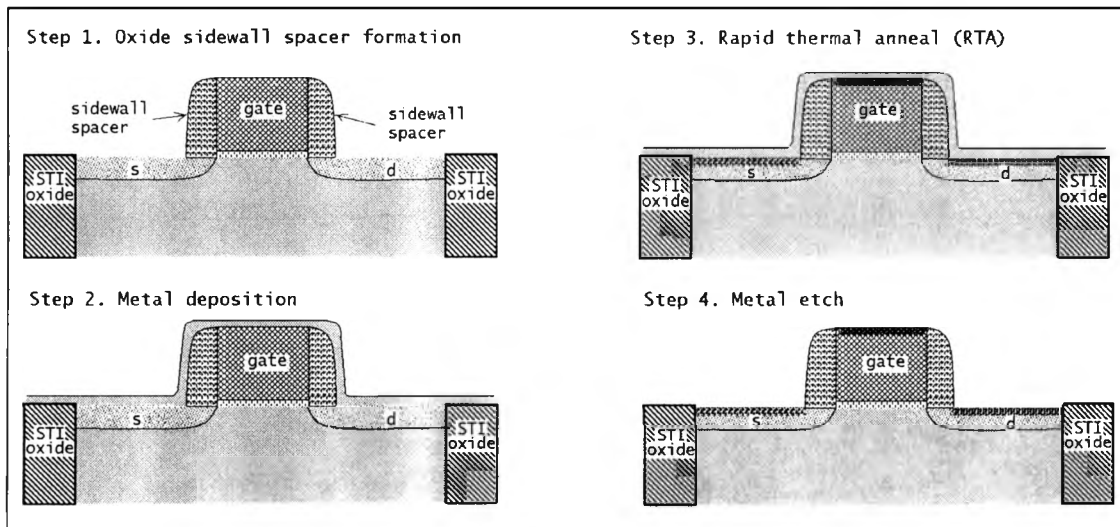


Figure 1. The salicide process.

Traditional methods of characterizing these silicides include X-ray diffraction (XRD) for structural analysis, Rutherford backscattering (RBS) for compositional data, and sheet resistance measurements of resistivity. These measurements can be done on silicide thin films grown on full wafers. An XRD spectrum from the sample is compared

to simulated spectra obtained by computational analysis of various crystal models. Once a good match is found, the crystal structure inferred from XRD can be verified by RBS compositional data and resistivity data. By combining such analyses, the phases present in the silicide are identified, and the kinetics of silicide formation are inferred from phase information of silicides formed at different temperatures.

Continuing development of reliable, low resistivity contacts depends upon accurately determining the physical properties of the silicide. Two analytical tools that are well suited to probing phase information are infrared and Raman spectroscopy. These methods probe the bond energies in the material and can be used to infer phase information about the material. This offers another independent source of data and increases the confidence level in any model formed by XRD and RBS data alone. In addition, these tools are faster than XRD. An infrared or Raman spectrum can typically be gathered from a metal silicide sample in a matter of minutes. This also suggests their use as in-line monitoring tools.

The species of dopant in the source and drain regions is one of the many parameters which affects the silicidation process. In this paper, I determined the phases of nickel silicide formed at different temperatures on two different types of wafers. I gathered the Raman and infrared spectra of six nickel silicide samples. Three samples were p-doped with boron and received RTA treatments at 380C, 450C, and 850C. The other three samples were n-doped with phosphorus and received the same RTA treatments. I analyzed the spectra obtained and compared it to published results to identify the phases present in each sample. I also compared the observed phase formation kinetics to published results. Finally, I offer suggestions for further research

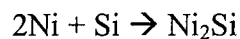
and use of Raman and infrared spectroscopy as in-line monitoring tools.

CHAPTER TWO:THEORY

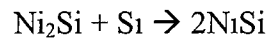
2.1 Formation and Structure of Nickel Silicide Contacts

Nickel monosilicide (NiSi) is a viable candidate to replace cobalt disilicide (CoSi₂) for active region electrical contacts in CMOS devices.² Its resistivity is in the range of 15 μohm-cm; this compares with that of cobalt disilicide (CoSi₂, 16-20 μohm-cm) and titanium disilicide (TiSi₂, 13-16 μohm-cm),³ the two most common materials used up to now in CMOS devices. In contrast to TiSi₂, its resistivity is stable on small line width structures,⁴ which is not true for TiSi₂. The temperature of formation of NiSi is lower than that of CoSi₂ and TiSi₂. Whereas NiSi begins to form on a <100> crystalline silicon substrate at 250C, the temperature of formation for CoSi₂ on the same silicon substrate is 500C; the low resistivity phase of TiSi₂ begins to form at 900C.⁵ Another advantage is that formation of NiSi is a one-step anneal whereas CoSi₂ and TiSi₂ require two sequential annealing steps to form their low resistivity phases.^{6,7} Another factor which makes NiSi attractive is that nickel consumes less silicon than both titanium and cobalt silicides in order to form the same silicide thickness. Relative silicon consumptions are 0.82 for nickel, 0.9 for titanium, and 1.04 for cobalt.⁸ One drawback to using NiSi is its low temperature of transition to the high resistivity phase NiSi₂. However, the thermal stability of NiSi has seen improvement with the use of metal barrier layers such as Pt or Co.^{9,10}

The formation of the nickel silicide contact begins with deposition of nickel metal onto the doped source and drain and polycrystalline gate. The next step is a thermal treatment that allows diffusion of atoms across the metal-silicon interface, at which point a silicide layer between the metal and silicon begins to grow. In the formation of nickel silicides, nickel is the dominant diffusing species. The mobility of the nickel atoms is much greater than the mobility of the silicon atoms. In transition metal-silicide diffusion reactions such as the reaction of Ni and Si atoms to form Ni₂Si, the rate of diffusion is controlled by a product of two factors: first, an overall diffusion coefficient; second, a “chemical term” which describes the free energy of the reaction¹¹



and likewise



The activation energy for the first reaction is 1.5 eV, and for the second reaction 1.7 eV.¹²

When the thickness of metal deposited is less than 200 nm on a <100> crystalline silicon substrate, the kinetics of silicide formation can differ from those observed in bulk silicide formation.¹³ Unlike the kinetics observed in bulk samples, the only phases formed in thin film samples are Ni₂Si, NiSi, and NiSi₂. Two phases which are absent, even though they are thermodynamically stable at the temperatures used, are Ni₃Si₂ and Ni₅Si₂. In addition to the absence of certain phases, thin film kinetics is characterized by the sequential formation of phases, layer by layer growth, and follows either diffusion

controlled or nucleation controlled kinetics.¹⁴ The requirements for the thin film limit are affected by the crystallinity of the silicon substrate. As the crystallinity of the substrate varies from single crystal to polycrystalline to amorphous, the adherence to layer by layer growth, sequential appearance of phases and absence of certain phases disappears.¹⁵

Diffusion-controlled kinetics is characterized by a steady film growth, described by the equation

$$T = (kt)^{1/2} \quad (\text{Equation 1})$$

where T is the thickness of the film, k is a kinetic parameter describing the reaction to form the film, and t is time. This type of kinetics describes the formation of both Ni₂Si and NiSi.¹⁶ In nucleation controlled kinetics, the formation of the new phase is limited by its high temperature of formation. At the temperature necessary to induce the phase transformation, diffusion is so rapid that the kinetics are hard to measure. This type of kinetics describes the formation of NiSi₂, the high resistivity phase nickel silicide.¹⁷

When forming nickel silicide in the thin film regime on <100> crystalline silicon, the first phase to appear is Ni₂Si at 200C. At 250C, a new layer of NiSi begins to form between the Ni₂Si layer and the silicon substrate once all the nickel is consumed to form Ni₂Si. Once all of the Ni₂Si is consumed to form NiSi, agglomeration into NiSi₂ can occur at 800C.¹⁸ All three silicides form with nickel as the dominant diffusing species; the nickel atoms move much farther than the silicon atoms.¹⁹ The process is shown in Figure 2.

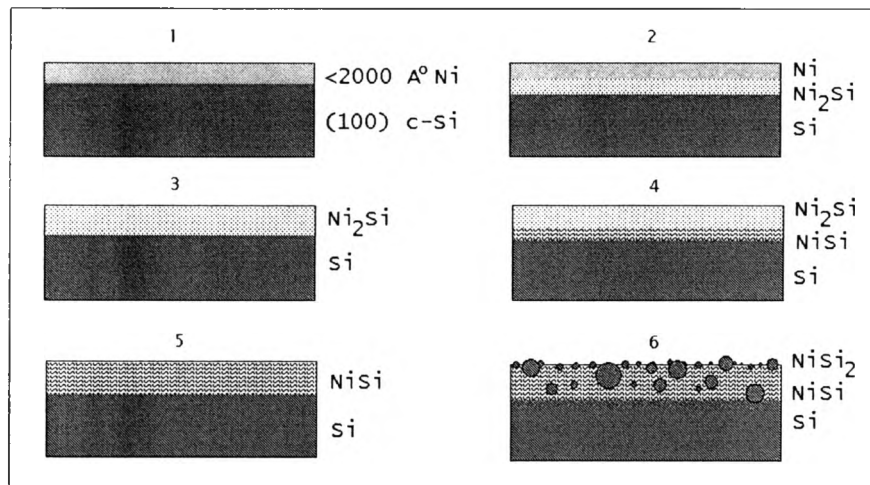


Figure 2. Thin film kinetics of nickel silicide growth.

In addition to the quality of the substrate and temperature of formation used, the species of dopant in the substrate will affect the thermal stability of the NiSi layer. The low resistivity phase NiSi will transform to NiSi₂ at a higher temperature on boron doped (p-type)silicon than on undoped silicon, and at a lower temperature on arsenic-doped (n-type) silicon.²⁰ It may be expected that the presence of phosphorous in the silicon will also alter the temperature of formation of silicides.

2.2 Theory of Raman spectroscopy

In order to produce a low resistivity ohmic contact to the active regions of the transistor, the thermodynamic parameters involved in the silicidation reaction must be controlled. The processes used to make the contacts are characterized by examining the crystalline quality and spatial extent of the silicide formed. Historically, silicide film properties such as crystal structure, degree of crystallinity, thickness of films and spatial extent of films have been measured with techniques such as XRD, RBS, X-ray photoelectron spectroscopy (XPS), TEM, and spectroscopic ellipsometry. XRD is used to determine the crystal structure. The XRD data acquired from a sample is compared to the spectra of several crystal models until a good match is found, and this match is

designated as the crystal structure of the sample. If multiple phases are present, the XRD pattern will appear as the superposition of multiple diffraction patterns. Even with this complication, the presence of numerous peaks in an XRD diffraction pattern allows the determination of structure, and XRD model data is readily obtained from the appropriate software.

The data acquisition process is usually time consuming since an XRD pattern can take several hours to obtain. Instead of continually relying on XRD for characterization, Raman spectroscopy offers a viable alternative to this time-consuming data acquisition technique. A Raman spectrum is taken from the sample in question, whose crystal structure can be determined from XRD. A Raman spectrum can be obtained relatively quickly, depending on the sample. Not all samples will exhibit Raman-active vibrational modes which means their Raman spectrum is relatively featureless. However, for phases such as NiSi that exhibit peaks in the Raman spectrum, Raman spectroscopy offers a way to validate structure and even has the possibility of being used as an in-line tool.²¹ In this way, a sample silicide can be scanned by Raman spectroscopy, and its spectrum can be compared to the Raman spectrum of a control sample. In addition, XRD suffers from poor spatial resolution, whereas Raman spectroscopy has a spatial resolution as low as 1.0 μm .²² Samples which do not have Raman active modes usually have IR active modes, so if there is no feature in the Raman spectrum, an IR spectrum can be taken in the same manner, with the additional requirement of the sample being in a high vacuum environment due to the strong absorbance of water vapor at infrared wavelengths. This Raman spectrum also offers detailed structural information because of the dependence of the activity of Raman peaks on the symmetry of the crystal unit cell. The same type of

modeling can be done for a Raman spectrum with appropriate software, which would be beneficial for getting detailed structural information similar to the way XRD provides structural data.

Raman and infrared spectroscopy are well suited to the task of characterizing nickel silicide growth. In this simple experiment, six silicide samples grown on crystalline silicon wafers were subjected to different RTA treatment temperatures. The characteristic spectra of the silicides present are reported in the literature.²³ In order to determine what phases of nickel silicide were present, the known peak positions of the silicides were compared to the peaks that appeared in the spectra of these samples. The key to characterizing silicides in this manner is that the spectra of reference samples are known.

Raman spectroscopy involves the inelastic scattering of a photon from excitations such as phonons in the material. It is a two step scattering process which allows the material to absorb a portion of the photon energy and convert it to a phonon. In an elastic scattering event, the atom absorbs the photon, and another photon with the same energy is emitted almost simultaneously. This is known as Rayleigh scattering. In an inelastic scattering event, the energy of the second photon is different from the original photon. This is known as Raman scattering. The energy levels involved in a Raman scattering event are shown in Figure 3. In a Raman scattering event, energy is transferred from the photon to the material or vice versa. The energy of the scattered photon is

$$\hbar\omega = \hbar\omega_0 - \hbar\omega_{vib} \quad (\text{Equation 2})$$

or

$$h\omega = h\omega_0 + h\omega_{vib} \quad (\text{Equation 3})$$

where ω_0 is the original photon frequency, ω_{vib} is the frequency of the vibration that interacts with the photon, and ω is the frequency of the scattered photon. Equation 2 represents a scattered photon which lost energy to the material, and it is referred to as a Stokes scattered photon. Equation 3 represents a scattered photon which gained energy from the material, and it is referred to as an anti-Stokes scattered photon.

The first step of the process is absorption of the photon by the atom, which puts the atom into a higher, “virtual” state. This virtual state is not an allowed energy level, and the atom stays in this state for a very short period of time. The second step is the creation of a phonon and a new photon that is shifted in energy, at which point the atom relaxes into a vibrational state different from the one it started in. The process does not involve the excitation of electronic energy levels. The change in vibrational energy level is only allowed for a transition in which the vibrational quantum number changes by ± 1 .

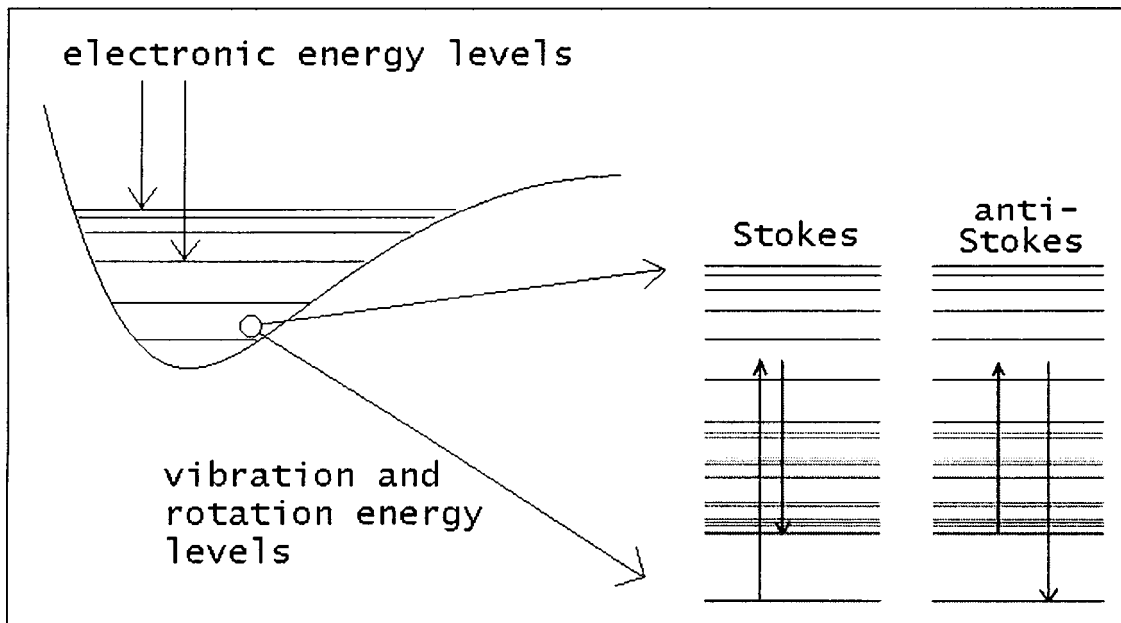


Figure 3. Energy levels involved in a Raman scattering event.

To examine how Raman spectroscopy probes the structure of the material, consider a crystal of nickel silicide, which has the same crystal structure as MnP, shown in Appendix B. The atoms in the crystal lattice oscillate about their equilibrium positions. At small displacements from equilibrium, the potential experienced by the atom is

$$V = \frac{1}{2}k(\Delta x)^2 \quad (\text{Equation 4})$$

where k is a constant characteristic of the bond strength between two atoms and Δx is the total displacement of the atom from its equilibrium position. In the classical harmonic oscillator, the total energy of the system is the sum of the kinetic and potential energies,

$$E = \frac{1}{2}(mv^2 + k(\Delta x)^2) \quad (\text{Equation 5})$$

and the frequency of vibration is

$$\omega = \sqrt{k/\mu} \quad (\text{Equation 6})$$

where μ is the reduced mass of the two atom system. The lowest energy of the classical harmonic oscillator is zero when the amplitude of vibration is zero.

To find the allowed energy levels of a quantum harmonic oscillator, the potential must be substituted into the Schrodinger equation. As shown in Appendix A, the wave function solutions take the form

$$\psi_n = \left(\frac{2m\omega}{\pi\hbar} \right)^{1/4} \frac{1}{\sqrt{2^n n!}} H_n(y) e^{-y^2/2} \quad (\text{Equation 7})$$

where $H_n(y)$ is a Hermite polynomial, ω is the frequency of vibration, and n is an integer

designating the vibrational state of the oscillator. The corresponding energy levels take the form of

$$E = (n + \frac{1}{2}) (\hbar \omega) \quad (\text{Equation 8})$$

where n is the vibration quantum number. The lowest energy level that the quantum harmonic oscillator can occupy is

$$\psi_0 = \left(\frac{2m\omega}{\pi \hbar} \right)^{1/4} \frac{1}{\sqrt{2}} e^{-\frac{m\omega x^2}{\hbar}/2} \quad (\text{Equation 9})$$

The energy of this state is $\hbar\omega/2$. The quantum harmonic oscillator will always have at least this amount of energy.

Many vibrational energies observed in Raman and IR investigations approximate the vibrational frequencies modeled by a harmonic potential. However, the actual potential experienced by the atoms involves higher order terms whose effects may become apparent at large atomic separations. The presence of higher order terms in the expression for the potential creates new energy levels that are not allowed in the harmonic oscillator approximation. The perturbation approach can be used to find the energy levels associated with these states. The amplitude of peaks in a Raman spectra which are due to the excitation of energy levels only allowed in the anharmonic approach are much smaller than harmonic peaks.

A typical Raman spectrum of NiSi appears in Figure 4.²⁴ This shows two peaks occurring at 217 cm^{-1} and 199 cm^{-1} . The spectrum is from a sample which also contains NiSi₂. Two broad peaks attributed to NiSi₂ also appear in the spectrum.

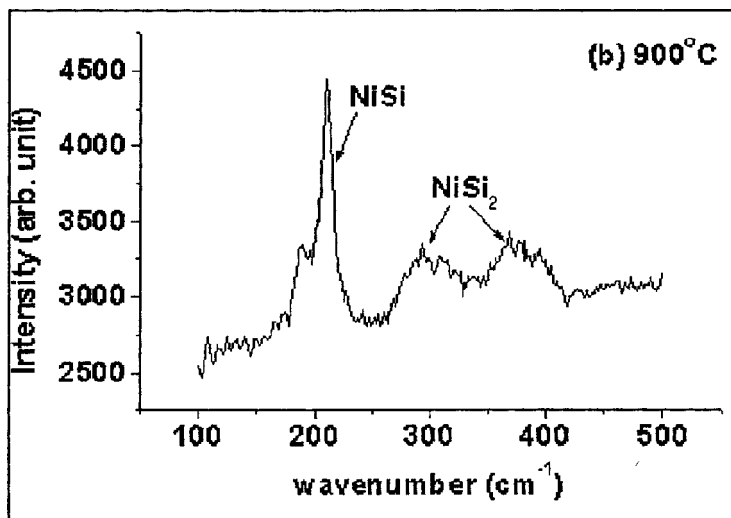


Figure 4. Typical Raman spectrum of NiSi.²⁴

The potential seen by the atom appears as in Figure 5, which shows the electronic, vibrational, and rotational energy levels available to the molecule.

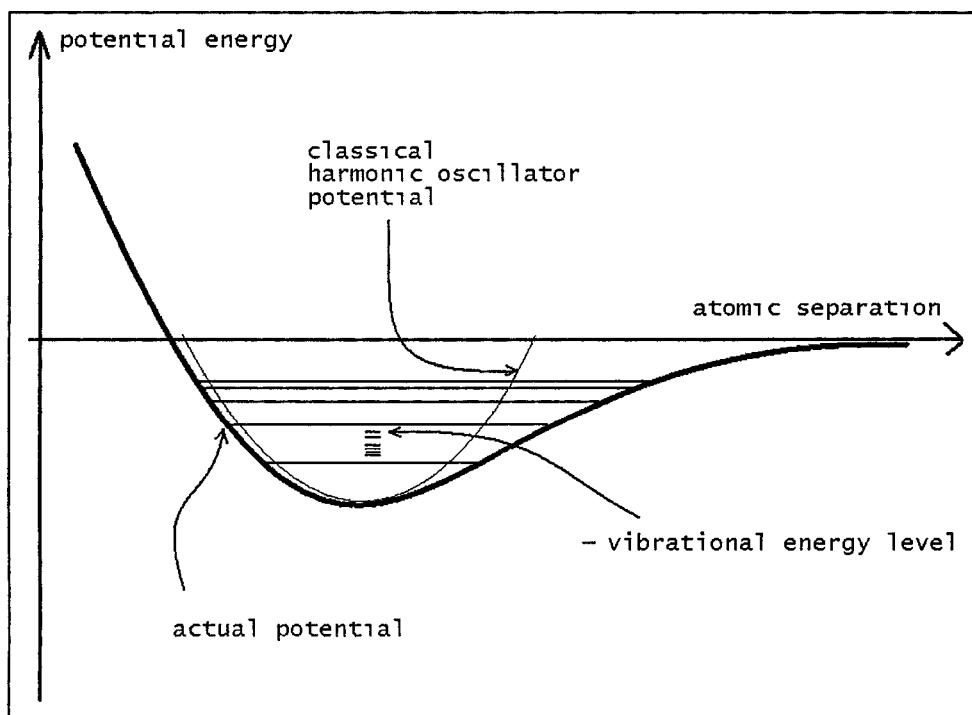


Figure 5. Potential energy of atoms in a solid.

The energy levels and frequencies of the quantum mechanical oscillator have now been found. In a real crystal solid, each atom is bound to more than one atom. The

equations of motion become more complicated when more springs are attached. However, the approach is the same. In a crystal with some degree of symmetry, these equations of motion can be simplified by viewing the atoms in crystal planes. Each degree of freedom results in another set of motion equations that can be solved. In a three dimensional crystal, this results in three separate solutions to the equations of motion if there is only one type of atom in the crystal. Then each atom offers a degree of freedom, so that the total degrees of freedom for the crystal is $3n$ where n is the number of atoms in the unit cell. Again, we can look at a single primitive cell and expand the solutions to represent all cells in the sample.

For each primitive cell with n atoms, there are a total of $3n$ degrees of freedom, because each atom can move in the three orthogonal directions x , y and z . Then, three of these degrees of freedom represent translation of the whole crystal. This is when the displacements of all atoms are in the same direction. Then there are three rotational degrees of freedom, or 5 for a linear molecule (very rare in solids but common in gases, such as CO_2). This results in a total of $3n-6$ degrees of freedom which represents the total number of discretely different vibrational modes. Take the example of hexane. Hexane has the chemical formula C_6H_{14} . There are a total of 20 atoms in hexane which means hexane will have a total of $3*20 - 6 = 54$ vibrational modes. The motions can be categorized as symmetric stretch, antisymmetric stretch, bending, wagging, and twisting. Some of the vibrations will be very similar in energy and vibrational frequency and hence will overlap in a vibrational spectrum. Each set of vibrations occurs at a different frequency. A visualization of the different types of vibrations available is represented in Figure 6 which shows a) the bending motion of a H-C-H bond and b) the antisymmetric

stretch of an H-C-H bond. The antisymmetric stretch of a C-H bond in an isolated molecule is typically in the 2900 cm^{-1} range, and the bending mode occurs at about 720 cm^{-1} .

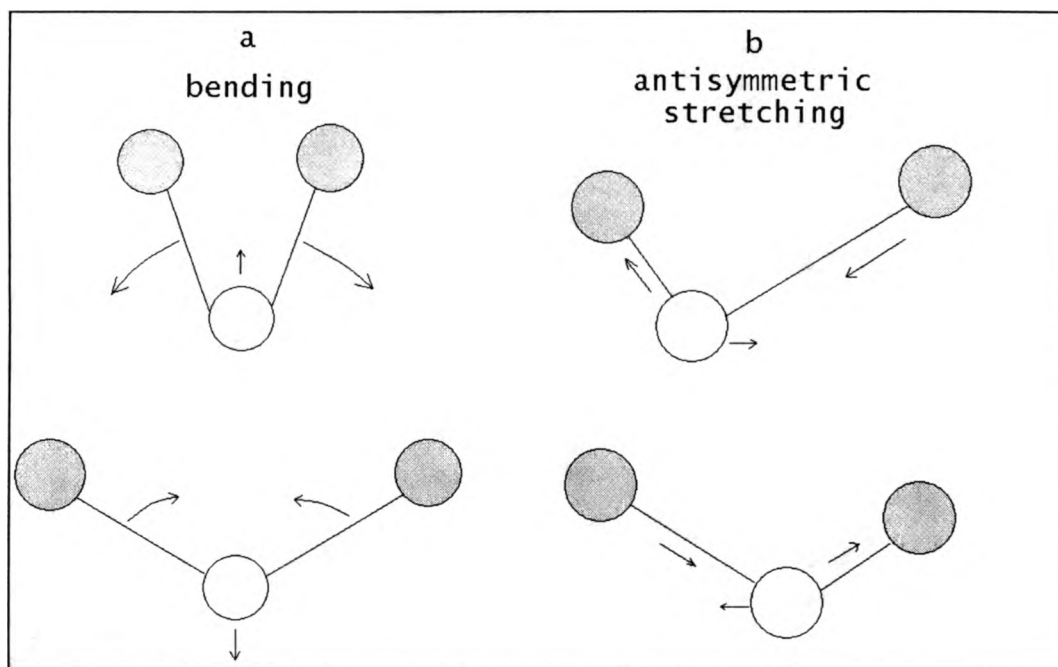


Figure 6. Vibrations of isolated molecules.

In a crystalline solid with more than one type of atom, more solutions for the motions of the atoms will result. In general, if there are N different atoms in the basis of the crystal lattice, there will be $2N$ independent solutions for the motion of the atoms. These different solutions are referred to as branches.

In a solid, the motions of the atoms are described by the presence of phonons, or quantized lattice vibrations. This allows the motion of the atoms to be described in terms of the type of motion involved. The motions of the atoms that are solutions to the equations of motion fall into two categories: An optical phonon is one in which adjacent atoms move opposite to each other, or approximately 180° out of phase. There are

longitudinal and transverse optical phonons, abbreviated LO and TO, respectively. An acoustic phonon is one in which adjacent atoms move together, or approximately 0° out of phase. There are also longitudinal and transverse acoustic phonons, abbreviated LA and TA, respectively. Optical phonons are much higher in energy than acoustic phonons since it takes more energy for the atoms to move in opposite directions. In a longitudinal phonon, the motion of the atoms is in the same direction as the propagation of the phonon. In a transverse phonon, the motion of the atoms is perpendicular to the direction of propagation of the phonon. This results in two identical phonons for each transverse mode, since there are two orthogonal directions for the atoms to vibrate in if they are moving perpendicular to the direction of phonon propagation. Both types of optical phonons will be close in energy, as will the two acoustic phonons. These phonons are described pictorially in Figure 7.

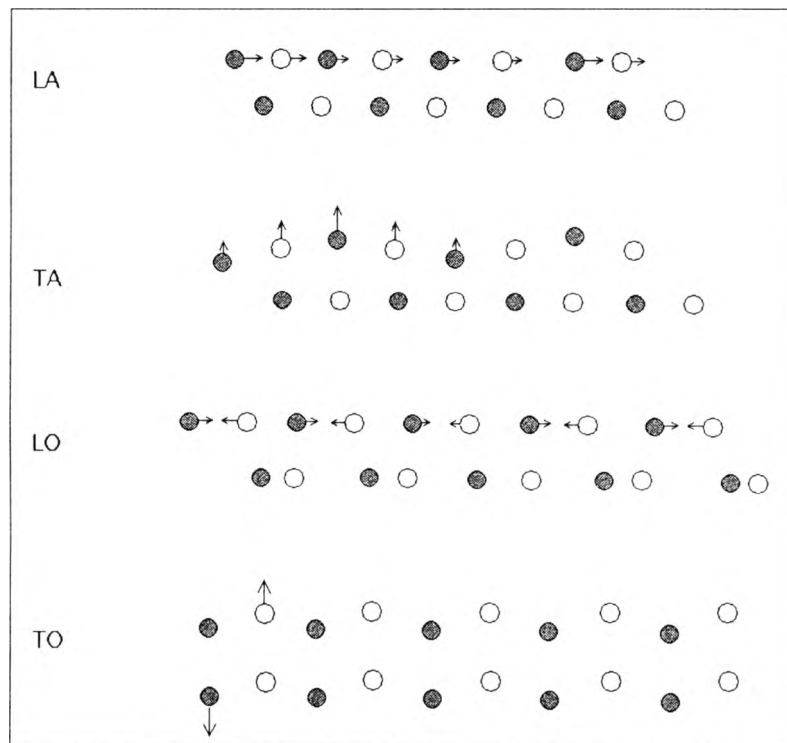


Figure 7. optical and acoustic phonons.

In a Raman experiment, the incoming photon is typically in the visible light range. The wave vector associated with such photons lies near the zone edge ($q=0$) for most solids, since the wavelength of the photon is much larger than the interatomic spacing. Therefore, most Raman scattering events take place from phonons whose wave vectors are near zero. Only a small percent of the light incident on a material is inelastically scattered. Thus the Raman (inelastically scattered light) signal is faint compared to the Rayleigh (elastically scattered light) signal.

Since the atom has a greater probability of being in the lower vibrational state, this state is more highly populated, and there is a greater probability that a phonon will be absorbed by the material, which corresponds to Stokes shifted light (red shifted). A smaller percentage of transitions occur from a higher vibrational state to a lower vibrational state, resulting in an anti-Stokes scattering spectrum. Both of these spectra are duplicates of each other, so an entire Raman spectrum shows identical peaks on either side of the Rayleigh position; the peaks on the Stokes scattered side (red-shifted photons) are higher in intensity than those on the anti-Stokes side. Raman spectra are commonly reported in wave number shift ($1/\lambda$, cm^{-1}) from the Rayleigh wavelength.

The appearance of peaks in a Raman spectrum is governed by the symmetry of the unit cell, which determines the change in polarizability of the bond involved in a vibration. The vibrating atoms in a bond set up an oscillating dipole which will radiate energy. This is necessary for the vibration to emit a second photon. In general, the dipole moment of a molecule depends on the electric field inducing the dipole and the polarizability of the bonds between the atoms. In three dimensions, the polarizability is described by the polarizability tensor:

$$\begin{bmatrix} \alpha_{xx} & \alpha_{xy} & \alpha_{xz} \\ \alpha_{yx} & \alpha_{yy} & \alpha_{yz} \\ \alpha_{zx} & \alpha_{zy} & \alpha_{zz} \end{bmatrix}$$

In the presence of an oscillating electric field $E = E_0 \cos(\omega_0 t)$, the dipole moment of the molecule P may be described as follows:

$$P(t) = \alpha E \quad (\text{Equation 10})$$

In the presence of the oscillating electric field, the polarizability of the molecule will oscillate in time as well. The frequency of oscillation will be equal to the natural frequency at which the bond vibrates, ω . The polarizability may be expressed as a combination of a static polarizability and an oscillating polarizability:

$$\alpha(t) = \alpha_0 + \alpha_1 \cos(\omega t) \quad (\text{Equation 11})$$

where α_0 is the static polarizability, α_1 is the oscillating polarizability, and ω is the natural frequency of the vibration. Combining the expressions for the electric field and the polarizability results in

$$P(t) = \alpha_0 E_0 \cos \omega_0 t + (\frac{1}{2}) \alpha_1 E_0 [\cos(\omega_0 + \omega)t + \cos(\omega_0 - \omega)t] \quad (\text{Equation 12})$$

The magnitude of the dipole moment oscillates in time, which results in three different frequencies being generated by the oscillating dipole. The two terms in brackets represent the Stokes and anti-Stokes emission by the dipole, respectively. A Raman active vibrational mode is one that allows the absorption of energy from the photon. In

order for the mode to be Raman active, the polarizability of the bond involved in the vibration must change during the vibration. Referring to Equation 12, this means that α_1 is not zero. This is known as the Raman selection rule.

In solids with a high degree of symmetry, most vibrational modes will be inactive in the Raman spectrum. The Raman spectrum reflects those vibrational modes that are not highly symmetrical. The crystal structure of Ni_2Si is the PbCl_2 structure which has 24 atoms per unit cell and is orthorhombic. The crystal structure of NiSi is the MnP structure which has 20 atoms per unit cell and is also orthorhombic. The crystal structure of NiSi_2 is the CaF_2 structure which is cubic and has 22 atoms per unit cell.²⁵ The crystal structures are shown in Appendix B. The high degree of symmetry in the NiSi_2 crystal structure will result in an absence of Raman active peaks, while the orthorhombic structures of NiSi and Ni_2Si allow the polarizability of vibrating bonds to change during the vibration, making them Raman active. For a crystal structure with N atoms per primitive unit cell, there will be $3N$ independent modes of vibration. For crystal structures such as the ones listed above, these modes will often have similar energies; this results in a broadened peak being observed in the Raman and IR spectra. Again, not all of the modes will be active due to symmetry considerations.

The anharmonicity of the potential seen by the atom has a two-fold effect. First, due to higher order terms in the expression for the potential, some vibrations are Raman active that are not active in the harmonic oscillator approximation. Second, the vibrational energy levels are closer together at higher energies. The first effect results in peaks that appear in the spectrum that are not predicted by the simple harmonic oscillator model. However, the probability of excitation of these vibrations depends on the square

of the transition matrix integral, which depends on the square of the wave function. These modes typically result in faint signals compared to the modes that are Raman active in the simple harmonic oscillator approximation. The second effect will be seen in “overtone” peaks in which the atom vibrates at twice the frequency as the original phonon. Anharmonicity perturbs the energy levels of higher energy modes so that the first overtone of a vibration does not occur at exactly twice the frequency as the normal mode. Again, overtone vibrations are relatively weak compared to the vibrations from which they are generated.

2.3 Raman Instrumentation

A Raman spectrometer consists of six main elements. The first is a monochromatic light source, or a filtered broadband light source. The second element is the focusing optics to focus the light source onto the sample, and for polarization studies, polarization optics to produce the desired polarization of light at the sample surface. The third element is collection optics for collecting the scattered light and focusing it onto a dispersing element. The fourth element is a dispersing element, such as a diffraction grating, and for polarization studies, polarization optics to probe the polarization of the scattered light. The fifth element is a detector that is sensitive to the wavelengths being probed. The sixth element is control hardware and software for controlling the position of the dispersing element and collecting the signal according to wavelength.

The first half of the spectrometer is used to get the exciting wavelength to the sample and collect and focus the scattered light onto the diffraction grating. The second part of the spectrometer, known as the monochromator, consists of a dark box that contains mirrors and the diffraction grating on a stage, and the entrance to the detector.

In order to subtract the excitation wavelength from the signal, a holographic notch filter is used which subtracts the wavelength directly. Another alternative is using a double or triple grating monochromator which disperses the light more so that the range of frequencies wanted is only imaged onto the detector. There is a trade-off of signal strength and spectral range.

The particular Raman system that I used has been patented by AMD. It is a combination of a LeicaNM200 light microscope with wafer inspection capabilities and a Renishaw Ramascope 2000. The laser light enters the spectrometer through a side entrance port. Then, the laser light travels through a polarizer that can be rotated to produce linearly polarized light at any degree relative to the plane of the sample. Next, the laser light is directed into a side entrance port to a microscope, and then onto a partially silvered mirror in the microscope. This allows some of the light to be directed to the view ports and the rest of the light to be directed onto the sample through an objective lens. The polarized laser light illuminates the sample which is placed on the microscope stage. The reflected and Raman scattered light is then gathered by the same objective lens. This light is filtered by a holographic notch filter (HNF) before it passes through more polarization optics which are used to a) decrease the signal from the silicon substrate and b) to study the polarization of the Raman scattered light. The light then passes through an entrance slit to the monochromator where it is dispersed by a diffraction grating. A final lens focuses the light onto a CCD detector. The schematic of the Raman spectrometer is shown in Figure 8.

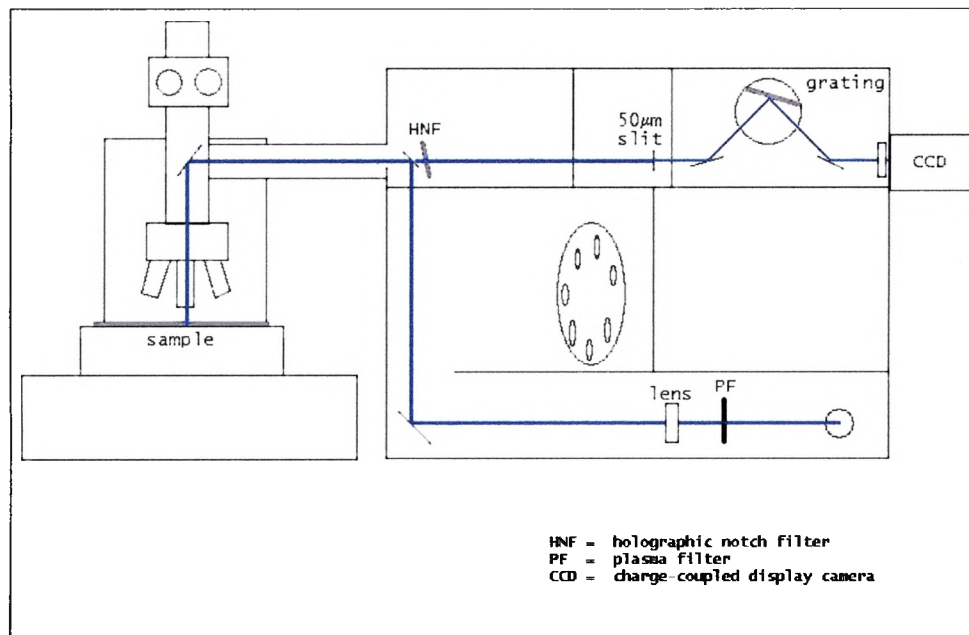


Figure 8. Schematic of Raman spectrometer.

The resolution of the spectrometer depends on four factors. First, the diffraction grating determines the angular separation of wavelengths. The optical path length of the light diffracted can be increased to enhance the spatial spreading of different wavelengths, but this is not the best way to get better resolution, since it takes up more space. Instead, the grating is chosen to get the resolution required for the particular application. Second, the detector is a CCD camera, so the resolution is affected by the pixel size of the camera. Limiting the area of the CCD detector used results in higher frequency resolution but decreases the signal strength. Third, the monochromator entrance slit limits stray light but also decreases signal strength. By narrowing the entrance slit and selecting a smaller area of the CCD to take a signal from, the frequency resolution increases. However, there is again a trade off between resolution and signal intensity. The highest resolution attainable on this instrument is 1.4 cm^{-1} .

2.4 Theory of Infrared Spectroscopy

An infrared spectrum measures the amount of infrared light absorbed by a sample over a range of frequencies. Most vibrational energies are in the range of 0.1 eV. This means that they will absorb infrared photons and convert them into vibrational energy. This contrasts with Raman spectroscopy because the entire photon is required to excite the vibration. By irradiating the sample with various wavelengths of light in the infrared region of the spectrum, the sample will absorb photons that match the frequency of vibrations of bonds in the material. The infrared selection rule is that the dipole moment of the bond involved in the vibration must change during the vibration. The transition matrix integral that determines whether a vibration is infrared active is²⁶

$$M_{nn'} = \int_{-\infty}^{\infty} \psi_{n'}^* \mu \psi_n dx \quad (\text{Equation 13})$$

The operator μ is the dipole moment of the two atoms involved in the vibration. The wavefunction $\psi_{n'}$ is the original vibrational energy level, and ψ_n is the excited vibrational energy level. In order for this integral to be nonzero, μ must be a function of x and therefore must change during the vibration. When the dipole moment changes during the vibration, this allows the electric field of the photon to couple to the oscillation of the nuclei through the oscillations of the electron cloud.

Raman and infrared spectroscopy are complementary to each other. Often, a vibrational mode that is not active in the infrared spectrum is active in the Raman spectrum, and vice versa. Molecules with a center of inversion will have vibrations that are mutually exclusive, that is, they will be either Raman active or IR active but not both

Some vibrations, generally those with high degrees of symmetry, will be inactive in both spectra.

2.5 FTIR Instrumentation

In practice, a broadband light source is used to irradiate the sample. This will enable the spectrum to be taken at all wavelengths at once. In Fourier Transform IR spectroscopy, this broadband source gets imaged onto the sample by a Michelson interferometer. The source light will pass through the interferometer beam splitter, and get split into two beams. The first beam will pass through the beam splitter and then to a stationary mirror, then back to the beam splitter, then through the beamsplitter again and on to the sample. The other beam will get imaged onto a moving mirror, then get reflected and pass through the beamsplitter again, and then onto the sample. At the sample, the resultant beam is a linear superposition (interferogram) of the two beams from the beamsplitter. The sample introduces a subtraction from the beam. The resultant beam passes to the detector.

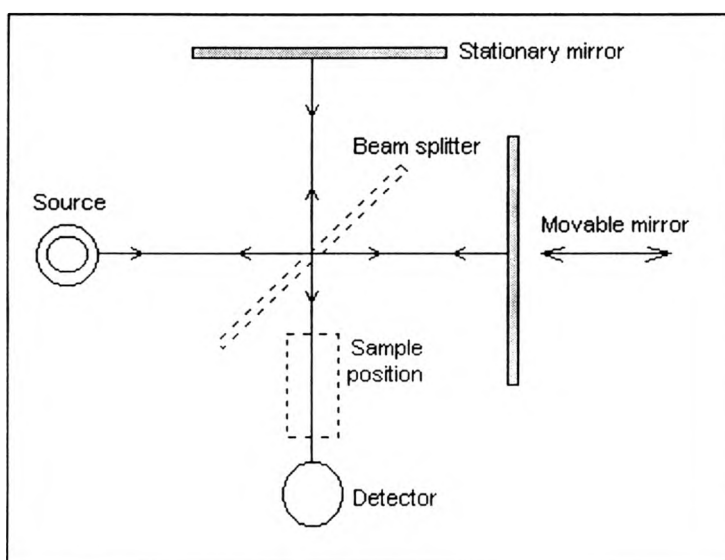


FIG 9. The Michelson interferometer.

At a given path difference between the two beams, the intensity of the signal at the detector is a result of the intensities at all wavelengths in the two beams, modulated by their linear combination. This intensity is described as

$$I'(\delta) = 0.5 * I(\nu)(1 + \cos(2\pi\delta/\lambda)) \quad (\text{Equation 14})$$

where δ is the optical path difference of the two beams, and λ is the wavelength. The DC component is not important. We just want to look at the varying component,

$$I(\delta) = 0.5 * I(\nu)(\cos(2\pi\delta/\lambda)) \quad (\text{Equation 15})$$

where ν is $1/\lambda$ or the wavenumber of the photon. There are other contributions to the intensity, such as the frequency dependence and uneven splitting of the beamsplitter, and the frequency response of the detector and signal amplifier. All this is put into a new modulating factor $B(\nu)$ which defines the spectral response of the spectroscopic system and the sample subtraction.

In order to gather a meaningful spectrum, first a reference scan is taken that accounts for the spectral characteristics of the source. Next, a phase scan is taken because the scan does not start at zero path difference. The phase scan is an adjustment made to the spectrum. Third, an apodization function is added to the spectrum. This accounts for not scanning from $-\infty$ to $+\infty$; the effect of this is that the integral does not extend to infinite path length. The apodization function puts more weight on the interferogram that is gathered at small path differences and less weight on the interferograms that are gathered at large path difference

The intensity at the sample depends on the optical path difference between the two beams. For totally destructive interference, the path difference is half of the

wavelength. In FTIR, a broadband source is used as the excitation probe, so the illumination at the sample is a sum of interferograms of all wavelengths present.

By moving the mirror and measuring the intensity at different optical path differences, the intensity at the detector is given by

$$I(x) = \int_0^{\infty} B(\sigma) (\cos(2\pi\sigma x)) d\sigma \quad (\text{Equation 16})$$

where $B(\sigma)$ is the intensity of light at wavenumber σ affected by the beamsplitter, collection optics, detector efficiency, and sample subtraction, and x is the optical path difference between the two beams.

By taking the inverse Fourier transform of the intensity as a function of path difference, we get the energy as a function of frequency;

$$B(\sigma) = \int_0^{\infty} I(x) (\cos(2\pi\sigma x)) dx \quad (\text{Equation 17})$$

the function $B(\sigma)$ gets plotted as the infrared transmission spectrum after being corrected by the reference scan. An absorbance spectrum is obtained by using the relation between absorbance and transmittance,

$$A = \log(1/T) \quad (\text{Equation 18})$$

Figure 10 is a schematic of the Bomem DA3 FTIR spectrometer.

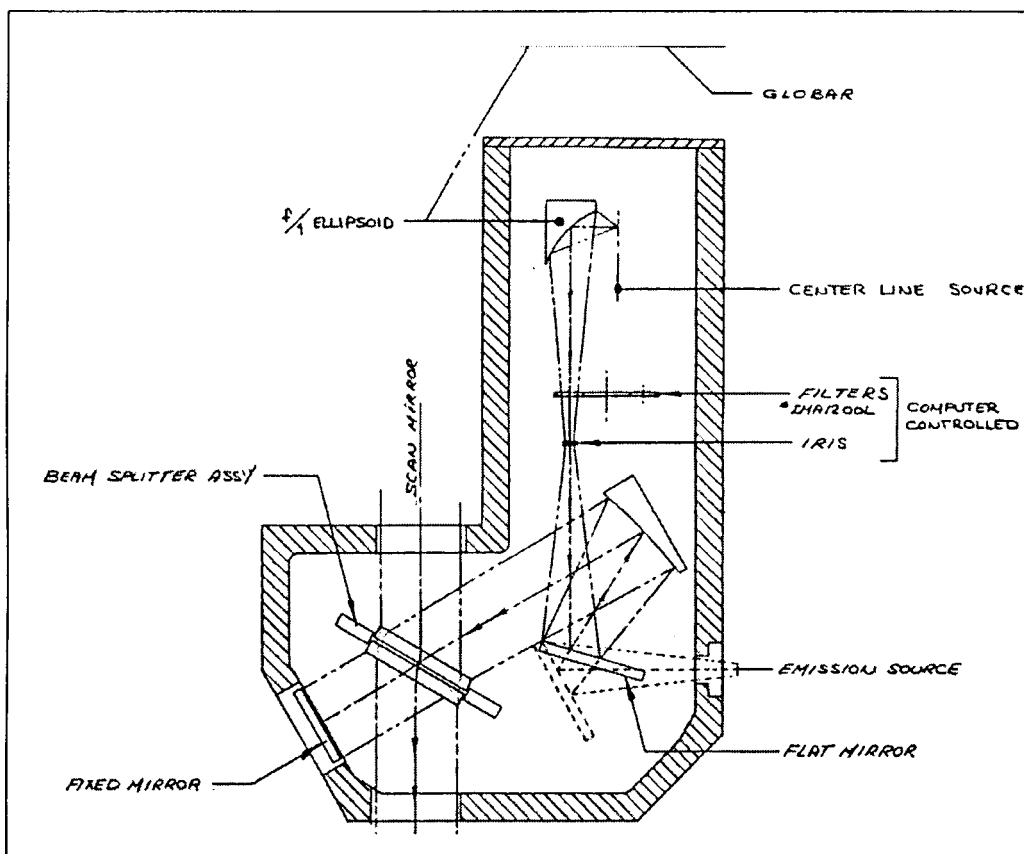


FIG 10. Schematic of FTIR spectrometer.²⁷

To complete the FTIR instrument, a HeNe laser is bounced off the back of the moving mirror to calibrate the path difference. Finally, water vapor in the atmosphere absorbs strongly in the infrared, so in order to take a spectrum, the sample and all optical components must be under vacuum at about 1 Torr.

CHAPTER THREE:EXPERIMENT

The sample preparation began with six <100> crystalline silicon wafers. The processing of all six samples used in this experiment began with a doping/dopant activation step. Three of the wafers were doped with boron, and the other three wafers were doped with phosphorous. All dopant concentrations were 10^{15} cm^{-3} . The next step was the deposition of 19 nm of nickel metal onto the wafer surfaces. Next, the wafers received an RTA treatment of thirty seconds. For both the phosphorous doped (n-type) and boron doped (p-type) wafers, three temperatures were chosen: 380C, 450C, and 850C. The final processing step was a metal etch using a HNO_3 dip to remove any unreacted nickel.

The Raman measurements were done on a Renishaw Ramascope 2000. The 488 nm wavelength of an Ar ion laser source was chosen for the excitation. The scattering geometry used was 180° backscattering. Data was gathered from 50 cm^{-1} to 650 cm^{-1} with a resolution of 1 cm^{-1} . A 50X objective lens was used which produced a circular beam $1.5 \text{ }\mu\text{m}$ across at the sample surface.

The FTIR measurements were taken on a Bomem DA.3 instrument with a KBr beamsplitter, Globar light source and reflection geometry. Data was gathered from 500 cm^{-1} to 5000 cm^{-1} with a resolution of 1 cm^{-1} .

CHAPTER FOUR:DATA

The FTIR spectra of the samples are presented below. All samples received an ultrasonic bath in an acetone/methanol mixture prior to scanning. However, peaks appear at 2850 cm^{-1} , 2920 cm^{-1} , and 2852 cm^{-1} in all samples, suggesting organic contamination. Besides these peaks, there were no other observable peaks which might be interpreted as absorbance of the sample. The spectral response of the KBr beam splitter is inefficient at low wavenumbers. This results in a higher signal to noise ratio from 500 cm^{-1} to 1500 cm^{-1} . The signal in this region does not represent absorption from the sample.

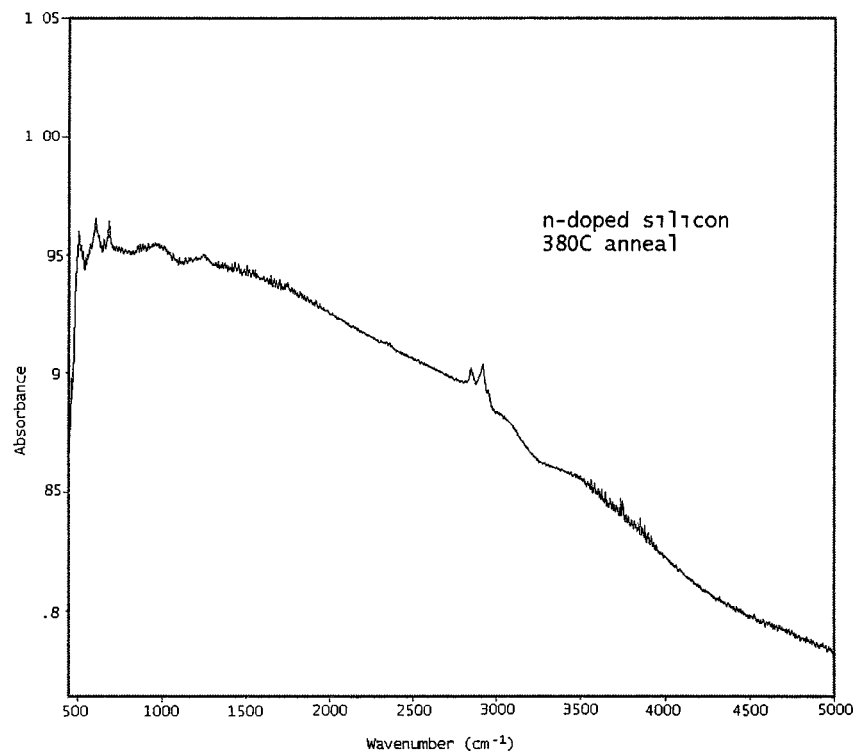


Figure 11. IR absorbance of n-doped, 380C annealed sample

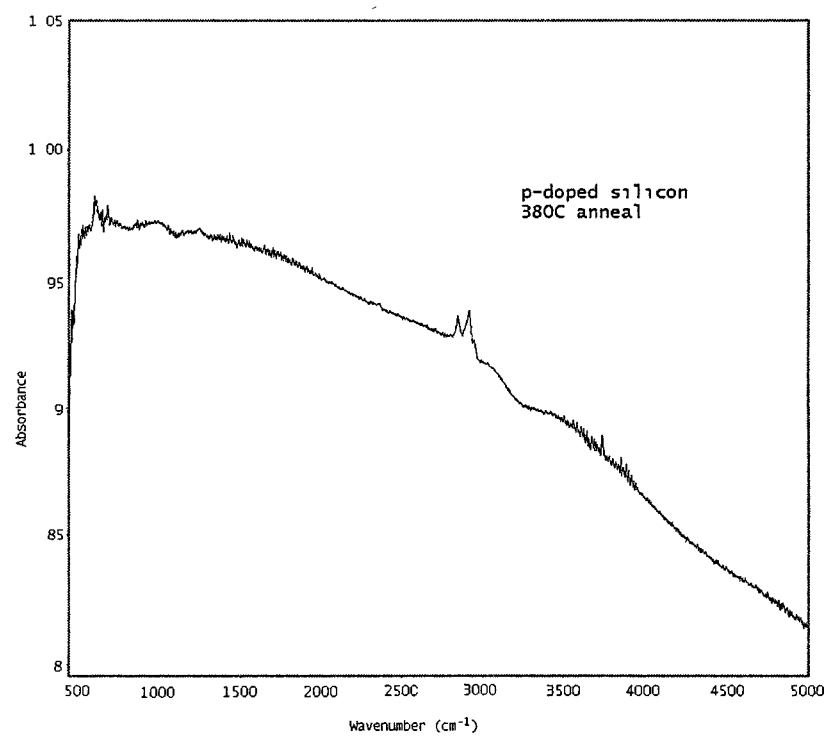


Figure 12. IR absorbance of p-doped, 380C annealed sample

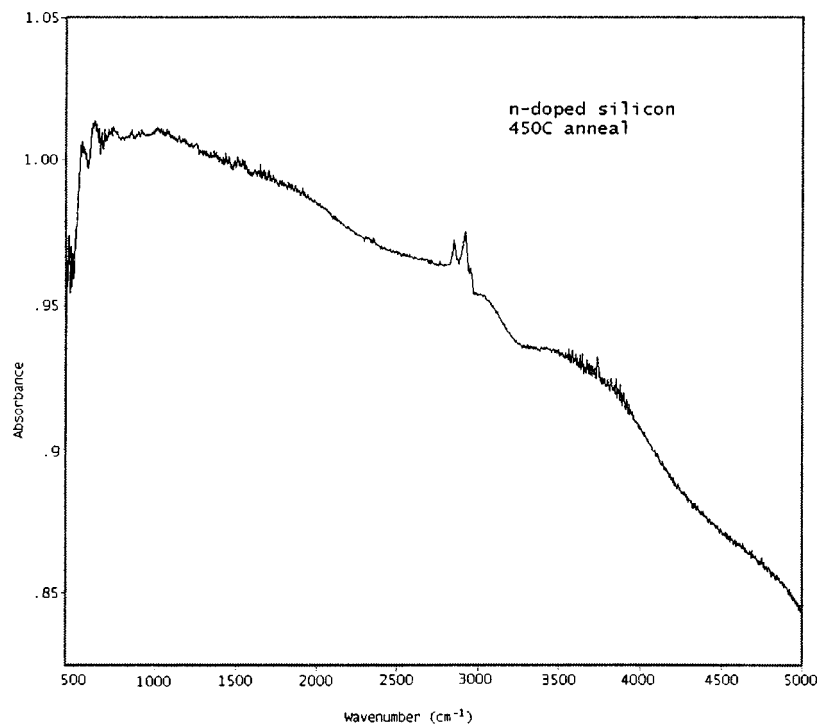


Figure 13. IR absorbance of n-doped, 450C annealed sample

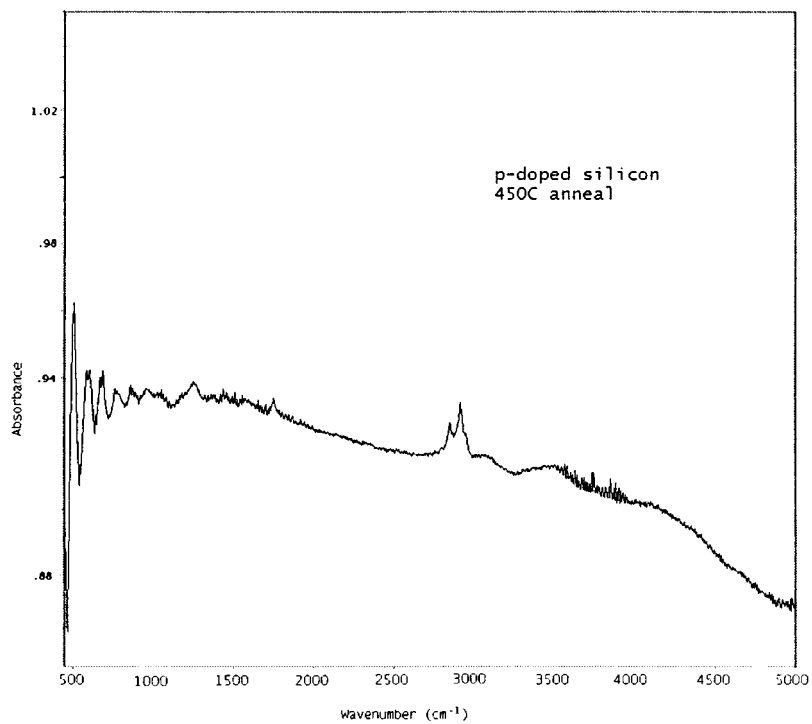


Figure 14. IR absorbance of p-doped, 450C annealed sample

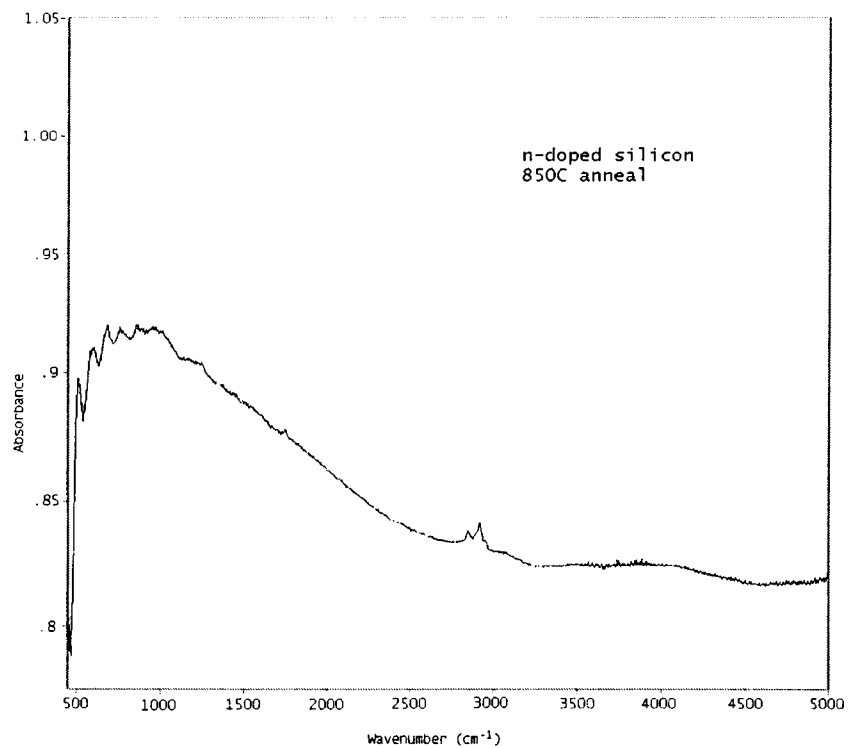


Figure 15. IR absorbance of n-doped, 850C annealed sample

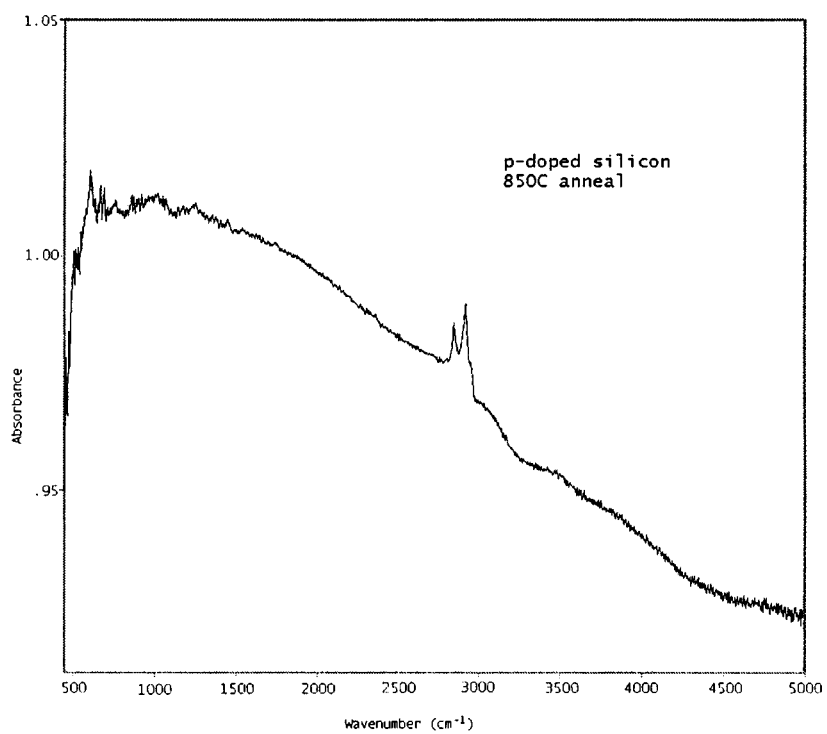


Figure 16. IR absorbance of p-doped, 850C annealed sample

The Raman spectra of the samples is presented below. In the samples annealed at 380C and 450C, a strong signal from the crystalline silicon substrate appears at 521 cm^{-1} . As the thickness of the silicide layer increases, the intensity of the substrate signal decreases. In the n-doped sample annealed at 850C, the substrate signal was so large that it went off the chart. In the p-doped sample annealed at 850C, the substrate signal is very small. This indicates agglomeration of the silicide film into particles. The spectrum taken on the n-doped sample most likely coincided with an area of exposed substrate. The spectrum taken on the p-doped sample most likely coincided with a large silicide particle.

The peaks at 197 cm^{-1} and 214 cm^{-1} are attributed to NiSi . These signals increase in strength from the 380C sample to the 450C sample. They do not appear in the samples annealed at 850C. The peak at 154 cm^{-1} that appears Figures 17,18, and 20 is attributed to Ni_2Si , but the signal strength suggests that there is very little Ni_2Si present. The broad peaks centered at 300 cm^{-1} and 360 cm^{-1} are attributed to NiSi_2 . These peaks appear in Figures 19 and 20.

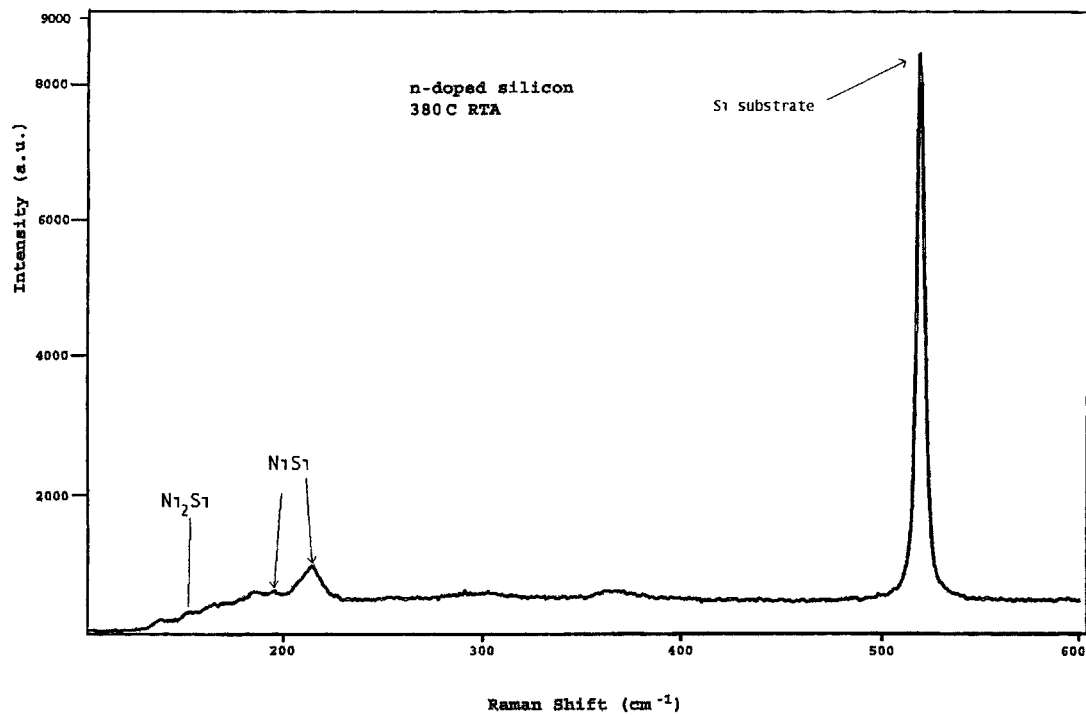


Figure 17. Raman spectrum of n-doped, 380C annealed sample

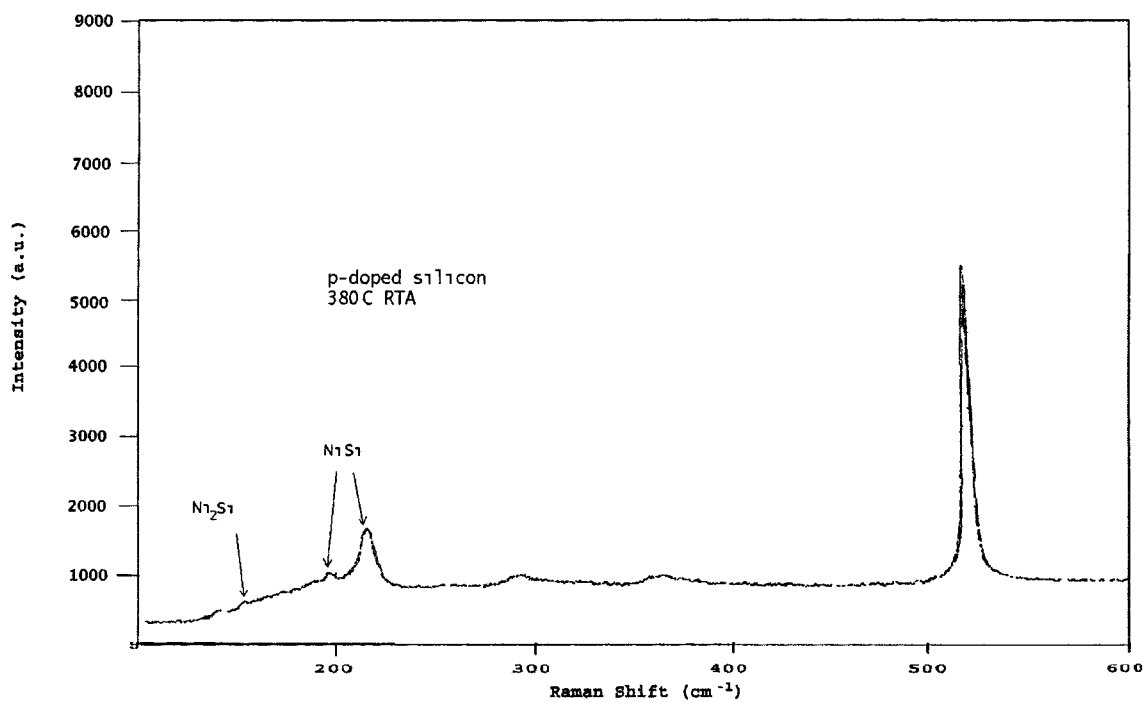


Figure 18. Raman spectrum of p-doped, 380C annealed sample

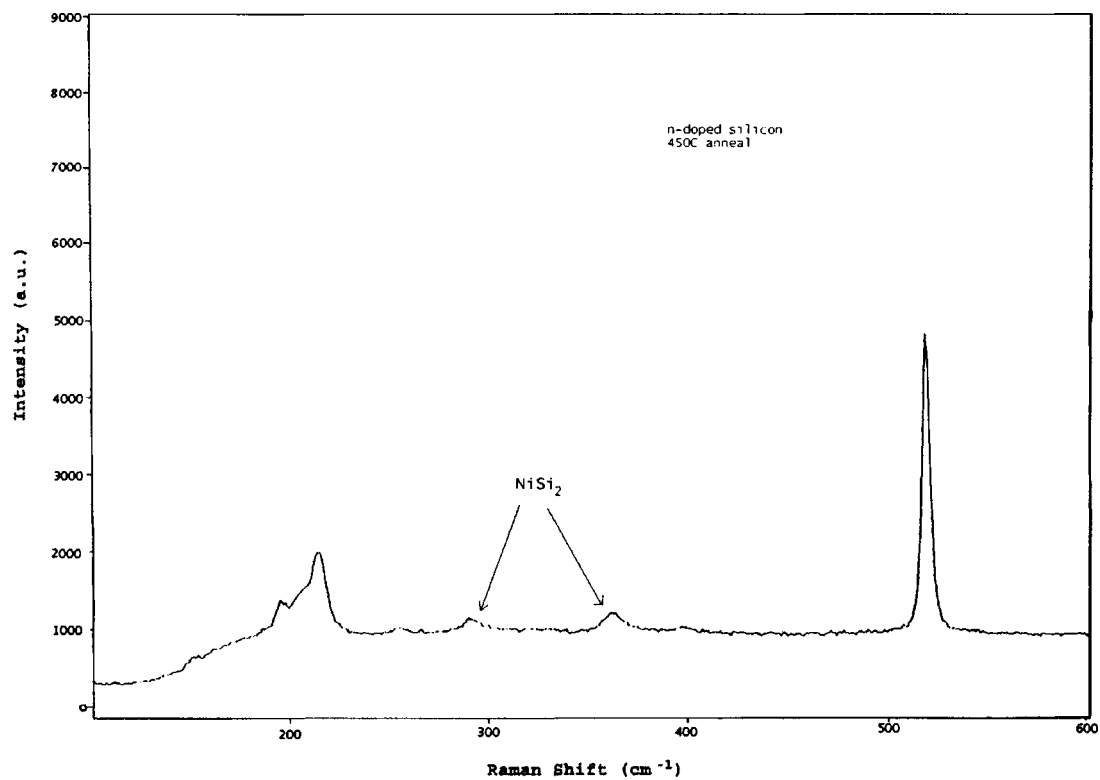


Figure 19. Raman spectrum of n-doped, 450C annealed sample

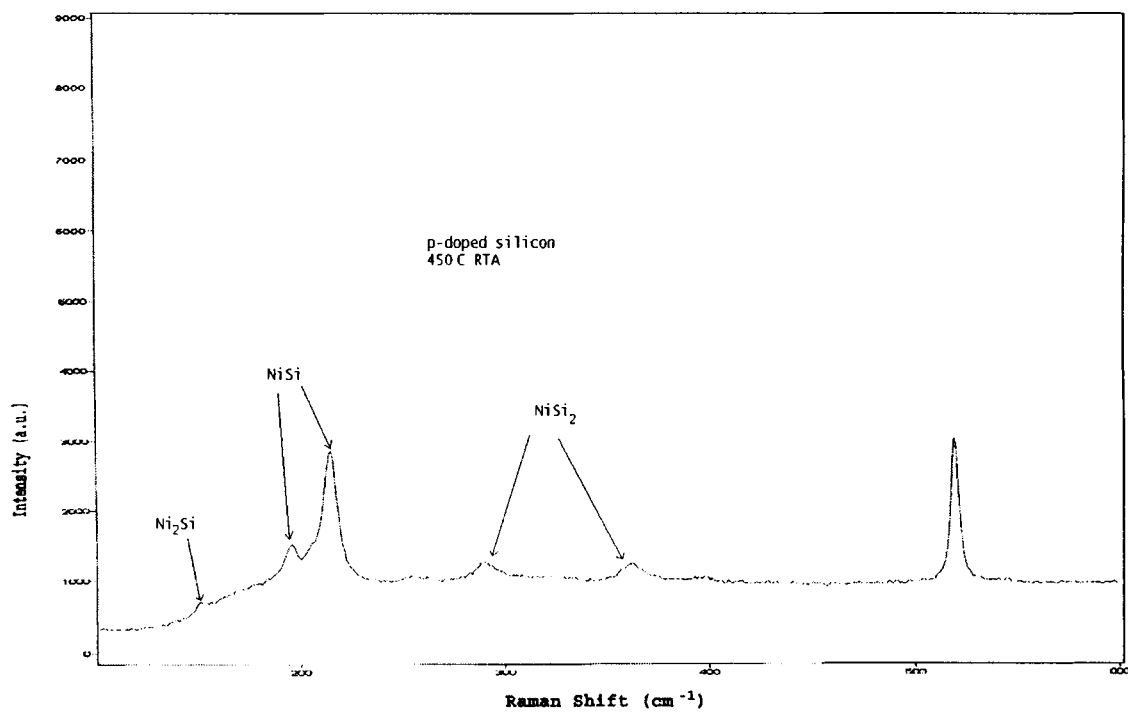


Figure 20. Raman spectrum of p-doped, 450C annealed sample

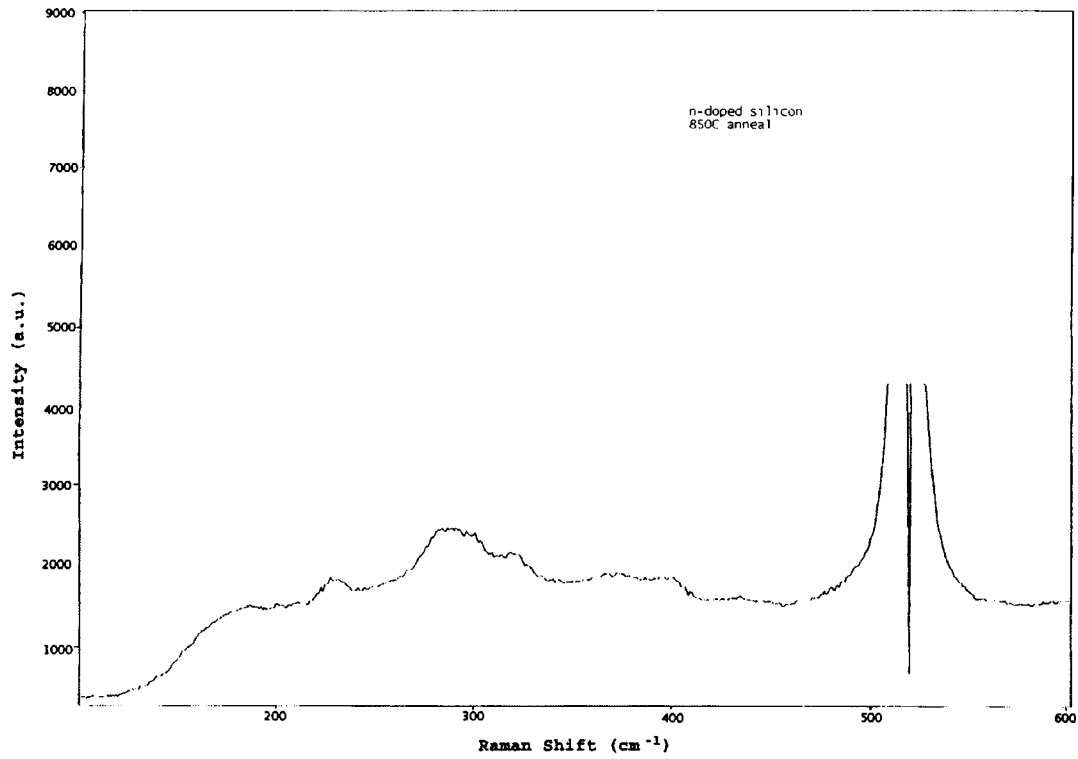


Figure 21. Raman spectrum of n-doped, 850C annealed sample

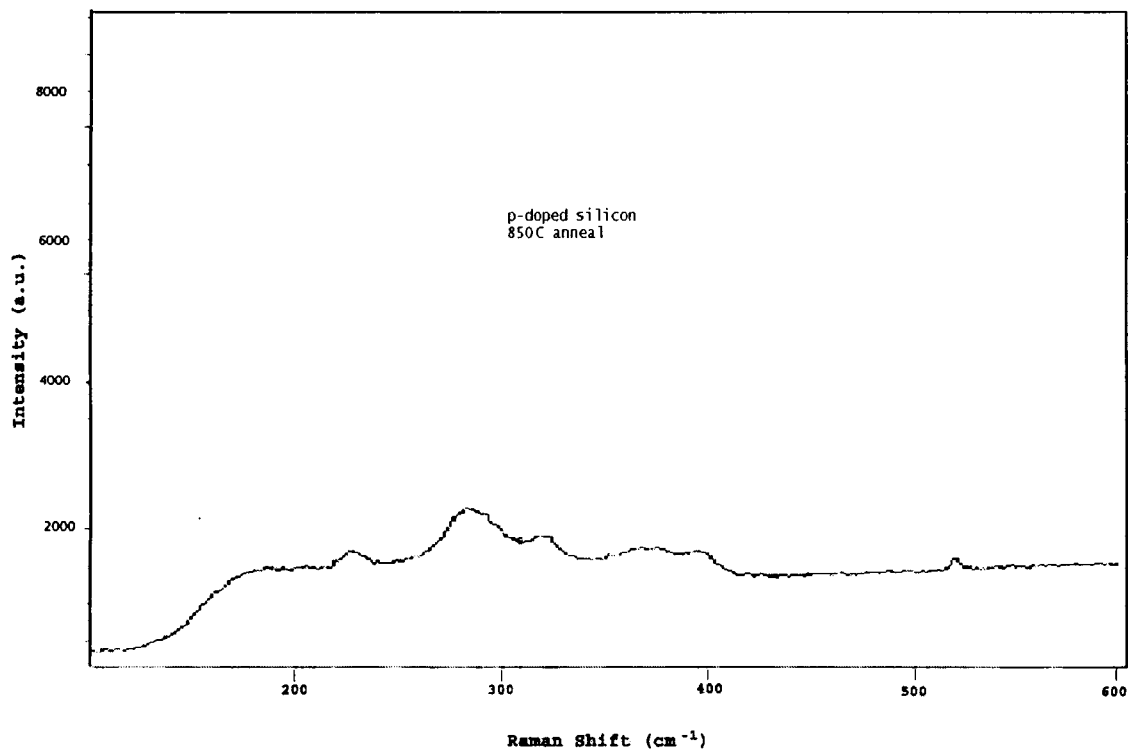


Figure 22. Raman spectrum of p-doped, 850C annealed sample

CHAPTER FIVE:RESULTS

Peaks in the Raman spectrum that have been attributed to NiSi are 199 cm^{-1} and 217 cm^{-1} .²⁸ These peaks, although shifted to 197 cm^{-1} and 214 cm^{-1} , occur in the Raman spectra of both types of samples annealed at 380C and 450C. This indicates the presence of NiSi in all four of these samples. In Figure 17, the Raman spectrum of the n-doped sample annealed at 380C shows the NiSi peak at 214 cm^{-1} but no visible peak at 199 cm^{-1} . In Figure 18, the Raman spectrum of the p-doped sample annealed at 380C contains both peaks. This should be expected. When referring to previously published results, the 199 cm^{-1} peak is usually weaker than the 214 cm^{-1} peak.²⁹ The peak intensity of the 214 cm^{-1} peak is greater in the p-doped sample annealed at 380C. In Figures 19 and 20, two peaks appear at 300 cm^{-1} and 360 cm^{-1} . These peaks are attributed to NiSi_2 .³⁰

The appearance of peaks attributed to NiSi agrees with the expectation that agglomeration into NiSi_2 does not occur until 800C and that formation of NiSi begins at 250C. However, thin film kinetics were not observed for these samples. For thin film kinetics, the NiSi layer does not begin to appear until all of the nickel has been consumed. In both the n-doped and p-doped samples, the intensity of the NiSi peaks increases from 380C to 450C which suggests that not all of the nickel was consumed in the 380C sample. In addition, the peaks that have been attributed to Ni_2Si , which are 100 cm^{-1} and 140 cm^{-1} ,³¹ did not appear at 380C which suggests that there was no Ni_2Si present in those samples. This means either that the Ni_2Si had already been consumed, or

that this phase was skipped altogether. Finally, peaks attributed to NiSi_2 appear in the samples annealed at 380C and 450C, alongside the peaks attributed to NiSi . The growth of NiSi in the presence of NiSi_2 indicates these two phases appearing together, instead of sequentially as was expected.

The difference in NiSi peak intensities between the n-doped and p-doped samples annealed at 380C suggests that dopant species has an effect on the rate of growth of the silicide. The amorphization of the silicon substrate is negligible due to the anneal to activate the implants. This means that any gain or loss of silicide growth rate is due primarily to more or less efficient diffusion mechanisms inherent in the different structures formed between B/Si and P/Si.

Peaks have also been attributed to the high resistivity phase, NiSi_2 . In the Raman spectrum a peak is expected at 263 cm^{-1} , and in the IR spectrum, a peak is expected at 373 cm^{-1} ; both of these values were obtained through the frozen-phonon calculation.³² The peak at 263 cm^{-1} was not observed in the Raman spectra of either of the samples annealed at 850C, and the peak at 373 cm^{-1} could not be observed due to the wavelength limitations of the MCT detector. However, agglomeration into the NiSi_2 phase can be assumed in the samples annealed at 850C. This is due to the disappearance of the peaks due to NiSi and the appearance of broad peaks that are characteristic of the higher symmetry NiSi_2 phase. Also, the silicon substrate peak intensity varies greatly between the n-doped and p-doped sample. This is most likely due to the obscuring of the substrate signal by the presence of a large NiSi_2 particle, or the absence of any silicide at all in the area being scanned, since the uniform NiSi layer had agglomerated into NiSi_2 particles.

The FTIR spectra of all six samples showed three peaks at 2850 cm^{-1} , 2920 cm^{-1} , and 2852 cm^{-1} . The presence of all three of these peaks in all the spectra is conspicuous, and might suggest organic contamination of the samples. Even though the samples were cleaned in an ultrasonic bath prior to scanning, the presence of these three peaks in all six samples strongly points to organic contamination. Otherwise, the FTIR spectra are featureless.

For future investigations of the effects of dopants on the kinetics of nickel silicide formation, it is suggested to study the Raman signals when the samples are annealed at a range of temperatures surrounding the expected transition temperatures. In this manner, the sequence of silicide formation can be seen. Agglomeration into NiSi_2 can be studied by annealing a sample at $>800\text{C}$ and taking Raman and IR spectra at various sites on the sample. The Raman data on my samples annealed at 850C suggest that the laser spot size is smaller than the agglomerated particle, so that the intensity of the silicon substrate signal would be directly affected by the presence of NiSi_2 . A quantitative investigation of the presence of silicides would require a knowledge of the scattering cross sections of all phases of interest. Then it can be shown through the Raman and IR spectra the volume ratio of phases present.

The polycrystalline nature of silicides can be seen qualitatively by the redshift and broadening of the peaks because the phonon dispersion curve for an optical phonon has a negative gradient when moving away from $q=0$. By probing an optical phonon in a material, the degree of crystallinity can be inferred by this redshift and broadening of the peak. The gradient of the curve is different for an acoustic branch and an optical branch. This is shown in Figure 23.

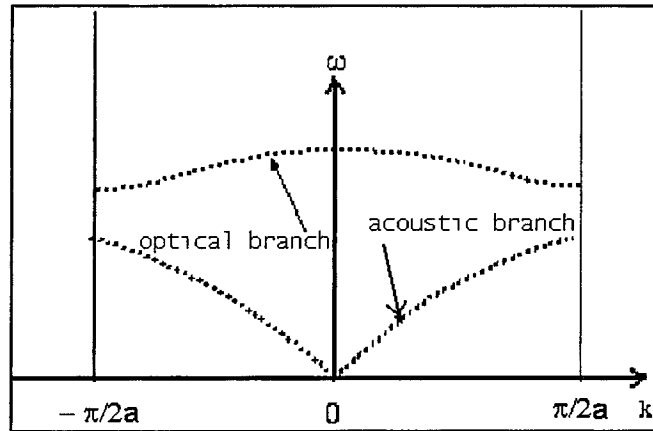


Figure 23. Typical phonon dispersion curve.

This requires a monocrystalline silicide sample, or a sample of known crystallinity, to produce a peak whose shape can be used as a reference.

Use of Raman and IR for in-situ characterization of silicides could be done with an in-line tool to monitor the quality of the films grown after the RTA step. In-situ real time monitoring of phase formation would be harder since the collection optics would intrude and influence the quality of the RTA step. Development of more efficient collection optics would afford the development of an in-situ real time monitoring of silicide phase formation.

APPENDIX A

EIGENSTATES AND ENERGIES OF A QUANTUM HARMONIC OSCILLATOR

The harmonic oscillator model gives an approximation to the motion of an atom that is bound to another atom by a chemical bond. According to this model, the atom will vibrate about its equilibrium position according to Hooke's Law.

The potential energy seen by the atom is

$$V = \frac{1}{2}(m\omega^2 x^2) \quad (\text{Equation A-1})$$

To find the eigenfunctions and energy eigenvalues associated with a one dimensional quantum harmonic oscillator, substitute this expression for potential energy into the Schrodinger equation:

$$\frac{-\hbar^2}{2m} \left(\frac{d^2\psi}{dx^2} \right) + \frac{1}{2}(m\omega^2 x^2)\psi = E\psi \quad (\text{Equation A-2})$$

Utilizing a Taylor series expansion, the solutions are

$$\psi_n = \left(\frac{2m\omega}{\pi\hbar} \right)^{1/4} \frac{1}{\sqrt{2^n n!}} H_n(y) e^{-y^2/2} \quad (\text{Equation A-3})$$

where

$$y = x \sqrt{\frac{m\omega}{\hbar}} \quad (\text{Equation A-4})$$

and $H_n(y)$ is a Hermite polynomial. The energy eigenvalues are

$$E = \left(n + \frac{1}{2} \right) \hbar \omega \quad (\text{Equation A-5})$$

These energy levels can be found directly by substituting for ψ in the Schrodinger equation, or by using the raising and lowering operators,

$$a_i^+ = \sqrt{\frac{m\omega_i}{2\hbar}} \left(x_i - \frac{\sqrt{-1}}{m\omega_i} p_i \right) \quad (\text{Equation A-6})$$

and

$$a_i = \sqrt{\frac{m\omega_i}{2\hbar}} \left(x_i + \frac{\sqrt{-1}}{m\omega_i} p_i \right) \quad (\text{Equation A-7})$$

respectively. By operating on the eigenstates of the oscillator with the raising operator, a new state is produced which represents the oscillator occupying a higher energy level.

The energy of the oscillator is found by applying the Hamiltonian to this new state:

$$H(a_i^+ |\psi\rangle) = (E + \hbar\omega)(a_i^+ |\psi\rangle) \quad (\text{Equation A-8})$$

This shows that the energy of the oscillator is $E + \hbar\omega$. Similarly, by operating on the eigenstate with the lowering operator, a new state is produced which represents the oscillator occupying a lower energy level with an energy of $E - \hbar\omega$:

$$H(a_i |\psi\rangle) = (E - \hbar\omega)(a_i |\psi\rangle) \quad (\text{Equation A-9})$$

The operator approach to the quantum harmonic oscillator also shows that the system cannot have an energy less than $\hbar\omega/2$. This is verified by expressing the Hamiltonian as

$$H = E = \hbar\omega \left(a_i^+ a_i + \frac{1}{2} \right) \quad (\text{Equation A-10})$$

and noting that $a_i^+ a_i = I$. Then,

$$\langle \psi | \frac{E}{\hbar\omega} - \frac{1}{2} | \psi \rangle \geq 0 \quad (\text{Equation A-11})$$

since this is just the inner product of ψ with itself, which must be nonzero. This shows that for any eigenfunction ψ , the energy of the oscillator must obey the inequality

$$E \geq \frac{\hbar\omega}{2} \quad (\text{Equation A-12})$$

The 3-dimensional quantum harmonic oscillator behaves like three independent harmonic oscillators. The Hamiltonian for the system is

$$H = \sum_{i=1}^3 \left(\frac{p_i^2}{2m} + \frac{1}{2} m\omega_i^2 x_i^2 \right) \quad (\text{Equation A-13})$$

There are three independent sets of raising and lowering operators for each dimension.

The total energy of the oscillator is

$$E = \sum_{i=1}^3 \hbar\omega_i \left(n_i + \frac{1}{2} \right) \quad (\text{Equation A-14})$$

In a symmetrical crystal, the individual energies for each dimension are equivalent, and the energy levels are degenerate. In a crystal with nonequivalent oscillator frequencies, this degeneracy is partially lifted.

APPENDIX B

CRYSTAL STRUCTURES OF NICKEL SILICIDES

Figure B-1 shows the crystal structure of nickel monosilicide, NiSi. The crystal structure is orthorhombic.

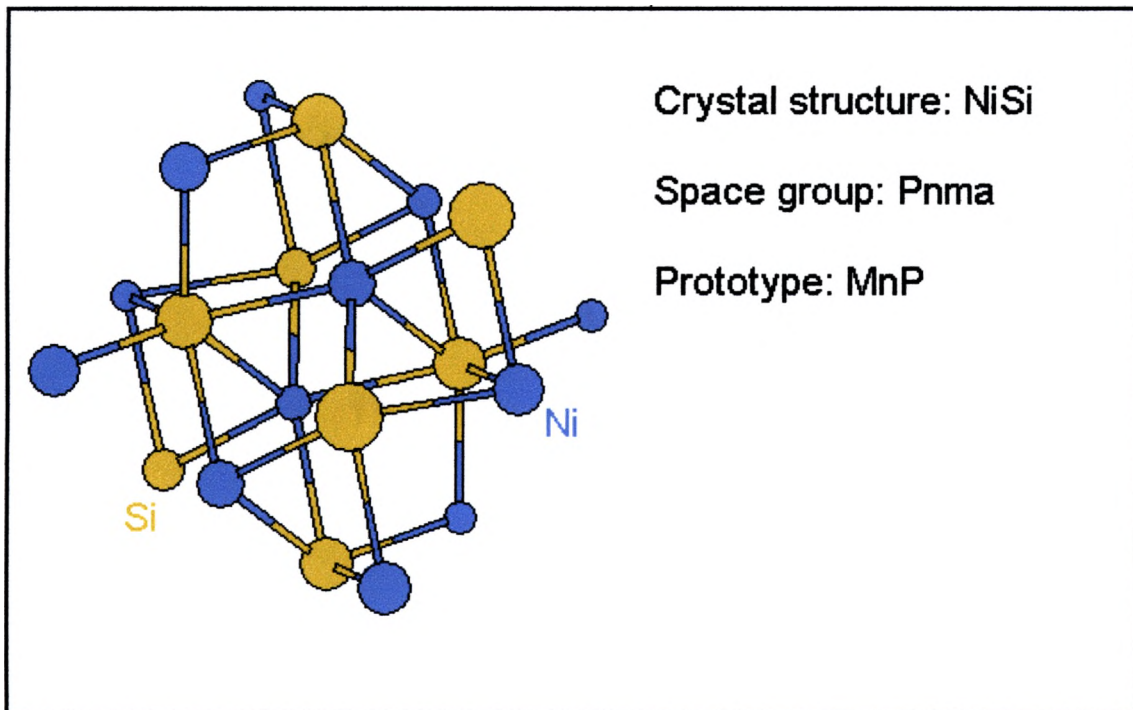


Figure B-1. Crystal Structure of NiSi.

The positions of the atoms in the unit cell of NiSi are as follows:

Primitive Vectors:

$$\mathbf{A}_1 = a \mathbf{X}$$

$$\mathbf{A}_2 = b \mathbf{Y}$$

$$\mathbf{A}_3 = c \mathbf{Z}$$

Basis Vectors:

$$\mathbf{B}_1 = +x_1 a \mathbf{X} + \frac{1}{4} b \mathbf{Y} + z_1 c \mathbf{Z} \quad (\text{Ni})$$

$$\mathbf{B}_2 = -x_1 a \mathbf{X} + \frac{3}{4} b \mathbf{Y} - z_1 c \mathbf{Z} \quad (\text{Ni})$$

$$\mathbf{B}_3 = (\frac{1}{2} - x_1) a \mathbf{X} + \frac{3}{4} b \mathbf{Y} + (\frac{1}{2} + z_1) c \mathbf{Z} \quad (\text{Ni})$$

$$\mathbf{B}_4 = (\frac{1}{2} + x_1) a \mathbf{X} + \frac{1}{4} b \mathbf{Y} + (\frac{1}{2} - z_1) c \mathbf{Z} \quad (\text{Ni})$$

$$\mathbf{B}_5 = +x_2 a \mathbf{X} + \frac{1}{4} b \mathbf{Y} + z_2 c \mathbf{Z} \quad (\text{Si})$$

$$\mathbf{B}_6 = -x_2 a \mathbf{X} + \frac{3}{4} b \mathbf{Y} - z_2 c \mathbf{Z} \quad (\text{Si})$$

$$\mathbf{B}_7 = (\frac{1}{2} - x_2) a \mathbf{X} + \frac{3}{4} b \mathbf{Y} + (\frac{1}{2} + z_2) c \mathbf{Z} \quad (\text{Si})$$

$$\mathbf{B}_8 = (\frac{1}{2} + x_2) a \mathbf{X} + \frac{1}{4} b \mathbf{Y} + (\frac{1}{2} - z_2) c \mathbf{Z} \quad (\text{Si})$$

$$a = 5.233 \text{ \AA}$$

$$b = 3.258 \text{ \AA}$$

$$c = 5.659 \text{ \AA}$$

Figure B-2 shows the crystal structure of Ni_2Si . The crystal structure is orthorhombic.

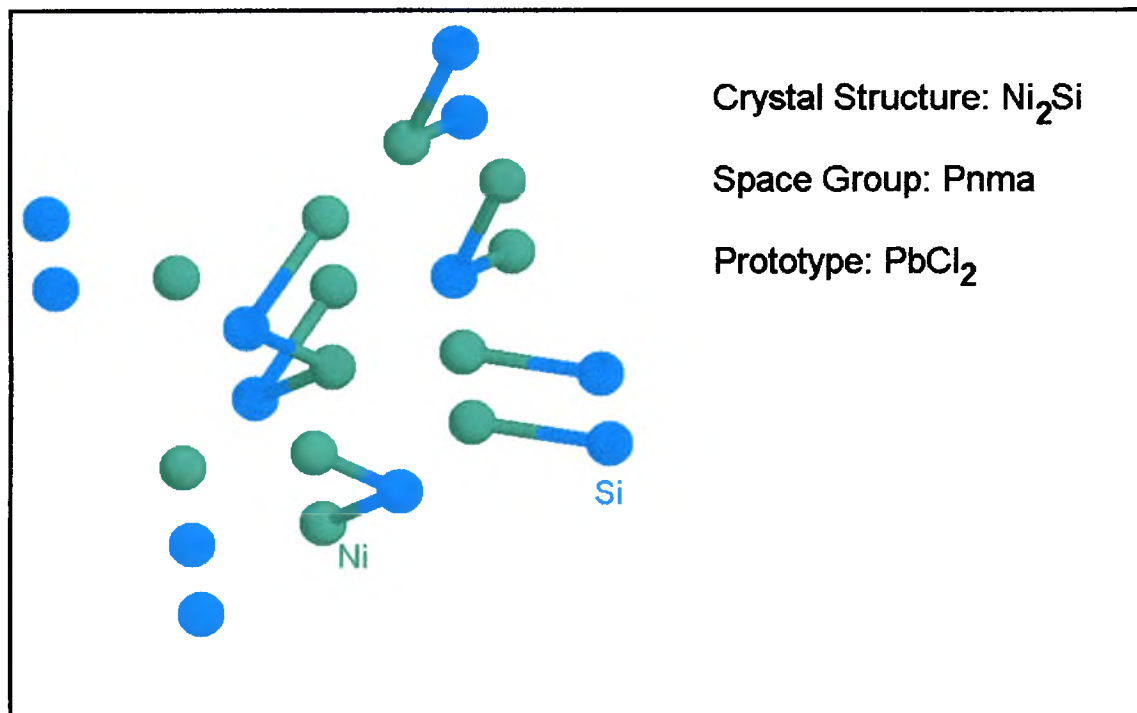


Figure B-2. Crystal structure of Ni_2Si .

The positions of the atoms in the unit cell of Ni₂Si are as follows:

Primitive Vectors:

$$\mathbf{A}_1 = a \mathbf{X}$$

$$\mathbf{A}_2 = b \mathbf{Y}$$

$$\mathbf{A}_3 = c \mathbf{Z}$$

Basis Vectors:

$$\mathbf{B}_1 = +x_1 a \mathbf{X} + \frac{1}{4} b \mathbf{Y} + z_1 c \mathbf{Z} \quad (\text{Si})$$

$$\mathbf{B}_2 = -x_1 a \mathbf{X} + \frac{3}{4} b \mathbf{Y} - z_1 c \mathbf{Z} \quad (\text{Si})$$

$$\mathbf{B}_3 = (\frac{1}{2} - x_1) a \mathbf{X} + \frac{3}{4} b \mathbf{Y} + (\frac{1}{2} + z_1) c \mathbf{Z} \quad (\text{Si})$$

$$\mathbf{B}_4 = (\frac{1}{2} + x_1) a \mathbf{X} + \frac{1}{4} b \mathbf{Y} + (\frac{1}{2} - z_1) c \mathbf{Z} \quad (\text{Si})$$

$$\mathbf{B}_5 = +x_2 a \mathbf{X} + \frac{1}{4} b \mathbf{Y} + z_2 c \mathbf{Z} \quad (\text{Ni-I})$$

$$\mathbf{B}_6 = -x_2 a \mathbf{X} + \frac{3}{4} b \mathbf{Y} - z_2 c \mathbf{Z} \quad (\text{Ni-I})$$

$$\mathbf{B}_7 = (\frac{1}{2} - x_2) a \mathbf{X} + \frac{3}{4} b \mathbf{Y} + (\frac{1}{2} + z_2) c \mathbf{Z} \quad (\text{Ni-I})$$

$$\mathbf{B}_8 = (\frac{1}{2} + x_2) a \mathbf{X} + \frac{1}{4} b \mathbf{Y} + (\frac{1}{2} - z_2) c \mathbf{Z} \quad (\text{Ni-I})$$

$$\mathbf{B}_9 = +x_3 a \mathbf{X} + \frac{1}{4} b \mathbf{Y} + z_3 c \mathbf{Z} \quad (\text{Ni-II})$$

$$\mathbf{B}_{10} = -x_3 a \mathbf{X} + \frac{3}{4} b \mathbf{Y} - z_3 c \mathbf{Z} \quad (\text{Ni-II})$$

$$\mathbf{B}_{11} = (\frac{1}{2} - x_3) a \mathbf{X} + \frac{3}{4} b \mathbf{Y} + (\frac{1}{2} + z_3) c \mathbf{Z} \quad (\text{Ni-II})$$

$$\mathbf{B}_{12} = (\frac{1}{2} + x_3) a \mathbf{X} + \frac{1}{4} b \mathbf{Y} + (\frac{1}{2} - z_3) c \mathbf{Z} \quad (\text{Ni-II})$$

$$a = 4.99 \text{ \AA}$$

$$b = 3.72 \text{ \AA}$$

$$c = 7.03 \text{ \AA}$$

Figure B-3 shows the crystal structure of NiSi_2 . The crystal structure is cubic.

Notice the high degree of symmetry.

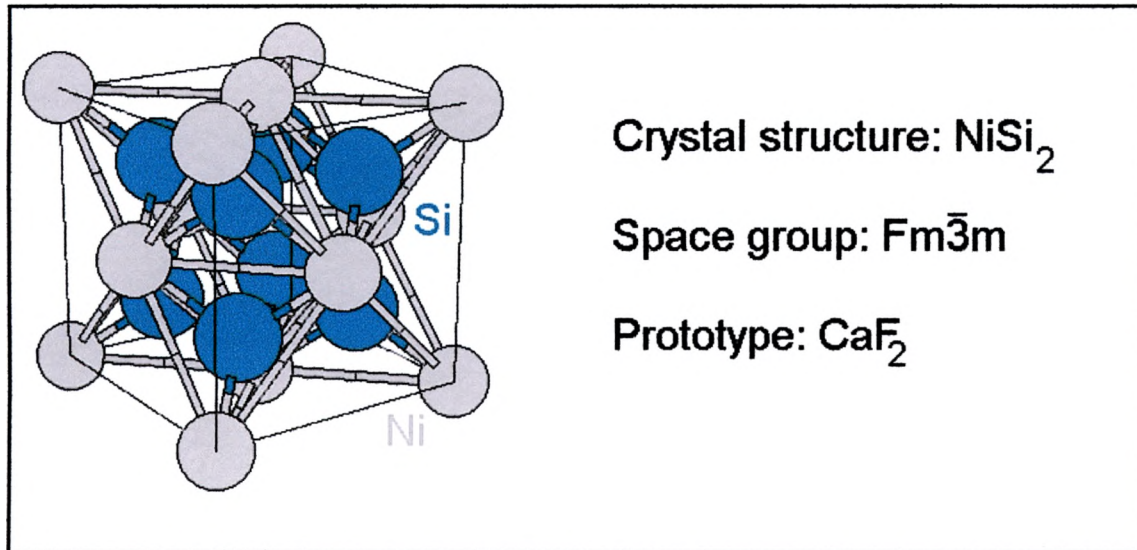


Figure B-3. Crystal structure of NiSi_2 .

The positions of the atoms in the unit cell of NiSi₂ are as follows:

Primitive Vectors:

$$\mathbf{A}_1 = \frac{1}{2} a \mathbf{Y} + \frac{1}{2} a \mathbf{Z}$$

$$\mathbf{A}_2 = \frac{1}{2} a \mathbf{X} + \frac{1}{2} a \mathbf{Z}$$

$$\mathbf{A}_3 = \frac{1}{2} a \mathbf{X} + \frac{1}{2} a \mathbf{Y}$$

Basis Vectors:

$$\mathbf{B}_1 = \quad \quad \quad 0 \quad \quad \quad (\text{Ni})$$

$$\mathbf{B}_2 = + \frac{1}{4} a \mathbf{X} + \frac{1}{4} a \mathbf{Y} + \frac{1}{4} a \mathbf{Z} \quad (\text{Si})$$

$$\mathbf{B}_3 = - \frac{1}{4} a \mathbf{X} - \frac{1}{4} a \mathbf{Y} - \frac{1}{4} a \mathbf{Z} \quad (\text{Si})$$

$$a = 5.43 \text{ \AA}$$

REFERENCES

- ¹ National University of Singapore courses website, http://courses.nus.edu.sg/course/phyweets/Projects99/MayJas/silicides_for_future_ics.htm, visited January 15, 2004.
- ² P.S. Lee, "Micro-Raman Spectroscopy Investigation of Nickel Silicides and Nickel (Platinum) Silicides", *Electrochemical and Solid-State Letters*, **3** (3), 2000, p. 153.
- ³ The Semiconductor Glossary website, www.semiconductorglossary.com, entry for "silicide, silicides", visited January 15, 2004.
- ⁴ M.C. Poon, "Resistivity and thermal stability of nickel mono-silicide", *Applied Surface Science* **157**, 29-34 (2000), p. 29.
- ⁵ P. Gas, "Formation of silicide thin films by solid state reaction", *Applied Surface Science* **73**, 153-161 (1993), p. 156.
- ⁶ R.J. Schreutelkamp, et. al, "2-Step Anneals To Avoid Bridging During Co Silicidation", *Applied Surface Science* **73** (1993), p. 162.
- ⁷ S. Kal and H. Ryssel, "Nondestructive analytical tools for characterization of thin titanium silicide films prepared by conventional and direct step silicidation with enhanced transition", *Journal of the Electrochemical Society* **146** (1999), p. 3440.
- ⁸ M. Tinani, "*In-situ* real-time studies of nickel silicide phase formation", *J. Vac. Sci. Technol. B* **19** (2), p. 376.

⁹ P.S. Lee, "Micro-Raman Spectroscopy Investigation of Nickel Silicides and Nickel (Platinum) Silicides", *Electrochemical and Solid-State Letters*, **3** (3) (2000), p. 154.

¹⁰ R.N. Wang, and J.Y. Feng, "Comparison of the thermal stabilities of NiSi films in Ni/Si, Ni/Pd/Si and Ni/Pt/Si systems", *Journal of Physics: Condensed Matter* **15** (2003) p. 1936.

¹¹ P. Gas and F.M. d'Heurle, "Kinetics of formation of TM silicide thin films: self-diffusion", IMEC, Leuven, Belgium 279-292 (1995), p. 281.

¹² F. d'Heurle, "Formation of thin films of NiSi: Metastable structure, diffusion mechanisms in intermetallic compounds", *Journal of Applied Physics* **55** (12), p 4217.

¹³ F. d'Heurle, "Formation of thin films of NiSi: Metastable structure, diffusion mechanisms in intermetallic compounds", *Journal of Applied Physics* **55** (12), 15 June 1984. P 4208.

¹⁴ P. Gas and F.M. d'Heurle, "Kinetics of formation of TM silicide thin films: self-diffusion", IMEC, Leuven, Belgium 279-292 (1995), p 279-280.

¹⁵ P. Gas, "Formation of silicide thin films by solid state reaction", *Applied Surface Science* **73**, 153-161 (1993), p. 160.

¹⁶ P. Gas and F.M. d'Heurle, "Kinetics of formation of TM silicide thin films: self-diffusion", IMEC, Leuven, Belgium 279-292 (1995), p 280.

¹⁷ P. Gas and F.M. d'Heurle, "Kinetics of formation of TM silicide thin films: self-diffusion", IMEC, Leuven, Belgium 279-292 (1995), p 280.

¹⁸ P. Gas, "Formation of silicide thin films by solid state reaction", *Applied Surface Science* **73** (1993), p. 156.

- ¹⁹ P. Gas and F.M. d'Heurle, "Kinetics of formation of TM silicide thin films: self-diffusion", IMEC, Leuven, Belgium 279-292 (1995), p 282-285.
- ²⁰ C.L. Shepard, et. al, "Stability of silicide films under post-annealing: a dopant effect", *Materials Reliability in Microelectronics* **1** (1991), p. 467.
- ²¹ Renishaw Application Note SPD/AN/093, Issue 1.0, "Imaging of Silicon Stress in Microelectronics Using Raman Spectroscopy", p. 1. November 2003.
- ²² Renishaw Technology Note SPD/TN/091, Issue 1.0, "Raman Imaging", p. 1. November 2003.
- ²³ P.S. Lee, "Micro-Raman Spectroscopy Investigation of Nickel Silicides and Nickel (Platinum) Silicides", *Electrochemical and Solid-State Letters*, **3** (3), 2000, p. 154.
- ²⁴ R.N. Wang and J.Y. Feng, "Comparison of the thermal stabilities of NiSi films in Ni/Si, Ni/Pd/Si and Ni/Pt/Si systems", *Journal of Physics: Condensed Matter* **15** (2003) p. 1939.
- ²⁵ Naval Research Laboratory - Center for Computational Materials Science – Crystal Lattice Structure Database, <http://cst-www.nrl.navy.mil/lattice/>, visited January 10, 2004.
- ²⁶ Dr. Scott Kirkby (University of Missouri-Rolla) spectroscopy lecture notes on the web, <http://web.umar.edu/~pchem/spec/pdf/spec.lecture14.winter2002.pdf>, visited September 16, 2003.
- ²⁷ Bomem DA.3 & DA.2 Spectrophotometer drawing manual, version 3, revision 1, December 1984, drawing number IOA000L.
- ²⁸ P.S. Lee, et. al., "Micro-Raman Spectroscopy Investigation of Nickel Silicides and Nickel (Platinum) Silicides", *Electrochemical and Solid State Letters*, **3** (3) (2000), p.

153

²⁹ R.N. Wang and J.Y. Feng, "Comparison of the thermal stabilities of NiSi films in Ni/Si, Ni/Pd/Si and Ni/Pt/Si systems", *Journal of Physics: Condensed Matter* **15** (2003) p. 1939.

³⁰ R.N. Wang and J.Y. Feng, "Comparison of the thermal stabilities of NiSi films in Ni/Si, Ni/Pd/Si and Ni/Pt/Si systems", *Journal of Physics: Condensed Matter* **15** (2003) p. 1939.

³¹ E. Kurimoto and H. Harima, "Raman study on the Ni/SiC interface reaction", *Journal of Applied Physics* **91** (2002) p. 10216.

³² L. Miglio, et. al., "Semiempirical Calculation of Structural and Dynamical Properties of Silicides in the Epitaxial Phases", *Physica Scripta* vol. T55, 81-85 (1994), p. 82.

VITA

Anita Reneé Acevedo was born in New Braunfels, Texas, on November 17, 1975, to Reynaldo and Francine Acevedo. After graduating from New Braunfels High School in 1994, she entered Texas State University-San Marcos. She received her bachelor's degree in physics from Texas State University in December 1999. In January 2000, she entered the Graduate College of Texas State University-San Marcos.

Permanent address:

540 Butcher St

New Braunfels, TX 78130

This thesis was typed by Anita Reneé Acevedo.